LRP 671/00 July 2000

Papers presented at the

27th EPS CONFERENCE ON CONTROLLED FUSION AND PLASMA PHYSICS

Budapest, Hungary
June 12 - 16, 2000

ISSN 0458-5895

LIST OF CONTENTS

High power ECH and fully non-inductive operation with ECCD in the TCV tokamak

S Coda, T P Goodman, M Henderson, F Hofmann, Z A Pietrzyk, O Sauter, S Alberti, C Angioni, K Appert, R Behn, P Blanchard, P Bosshard, R Chavan, A Degeling, B P Duval, D Fasel, A Favre, I Furno, P Gomez, P Gorgerat, J-P Hogge, P-F Isoz, B Joye, P Lavanchy, J B Lister, X Llobet, J-C Magnin, A Manini, B Marlétaz, P Marmillod, Y Martin, An Martynov, J-M Mayor, J Mlynar, J-M Moret, P Nikkola, P J Paris, A Perez, Y Peysson[†], R A Pitts, A Pochelon, H Reimerdes, J H Rommers, E Scavino, A Sushkov[‡], G Tonetti, M Q Tran, H Weisen, A Zabolotsky

Centre de Recherches en Physique des Plasmas, Association EURATOM - Confédération Suisse, Ecole Polytechnique Fédérale de Lausanne, CH-1015 Lausanne, Switzerland

[†]*Département de Recherches sur la Fusion Contrôlée, Association EURATOM-CEA, CEA/Cadarache, 13108 Saint Paul-lez-Durance Cédex, France*

[‡]*INF, Russian Research Center, Kurchatov Institute, Moscow, Russian Federation*

Abstract

Experiments with high power electron cyclotron heating (ECH) and current drive (ECCD) in the TCV tokamak are discussed. Power up to 2.7 MW from six gyrotrons is delivered to the tokamak at the second harmonic frequency (82.7 GHz) in X-mode. The power is transmitted to the plasma by six independent launchers, each equipped with steerable mirrors that allow a wide variety of injection angles in both the poloidal and toroidal directions. Fully non-inductive operation of the tokamak has been achieved in steady state, for the full 2 s gyrotron pulse duration, by co-ECCD with a highest current to date of 210 kA at full power. The experimentally measured ECCD efficiency agrees well with predictions obtained from linear modeling. We have observed

that the highest global efficiency attainable at a given power is limited by stability constraints. While the efficiency is maximum on the magnetic axis, a disruptive MHD instability occurs when the width of the deposition profile is lower than a minimum value, which increases with total power. Many ECCD discharges display a high level of electron energy confinement, enhanced by up to a factor of two over the Rebut-Lallia-Watkins (RLW) scaling law, which by contrast is well satisfied in Ohmic conditions. The longest confinement times (up to 4 times RLW) are observed with launching geometries that prevent the onset of sawtooth oscillations through current profile modification. Central electron heat diffusivities comparable to Ohmic levels are obtained in these scenarios, with electron temperatures in excess of 10 keV.

1. Introduction

Electron cyclotron heating (ECH) is an attractive technique for supplying energy to plasmas in thermonuclear regimes, owing to its high efficiency and localized deposition and to the high power throughput and modest space requirements of the launching structures. In recent years, substantial advances in the development of long pulse, high power gyrotron sources have significantly broadened the scope of this technique in the context of nuclear fusion research, particularly in tokamaks. ECH experiments can now be performed in quasi-steady-state, i.e., for times longer than all characteristic times in the plasma, and with power levels far exceeding the Ohmic heating component [1].

Electron cyclotron waves are also utilized for current drive (ECCD). This method is ideally suited for current profile control, thanks to its good efficiency combined with the high degree of localization and ease of positioning of the current source. Profile control is a key ingredient in prospective reactor operation, both in the conventional tokamak configuration, for MHD stabilization purposes, and in the so-called "advanced tokamak" configuration, for optimization of performance in steady state.

The first demonstration of steady-state operation in a tokamak with the toroidal current sustained entirely by ECCD has been recently performed in TCV (Tokamak à Configuration Variable), with an injected power of 1.35 MW and a driven current of 123 kA [2]. In this paper we report on the extension of these studies to power levels of 2.7 MW and driven currents of 210 kA.

Enhanced central confinement has been observed in TCV with counter-ECCD (antiparallel to the plasma current) on axis, with central temperatures and confinement times larger by a factor of two than with co-ECCD or pure ECH. With the aid of numerical transport modeling, this effect has been attributed to the inhibition of sawtooth oscillations achieved with this configuration, combined with heating in the centre where diffusivity is lowest [3]. More recently, different combinations of launching geometries, ECCD components and power waveforms have been devised to retain the high confinement while improving the MHD sta-

bility properties of the plasma [4]. The common factor in all these scenarios is the presence of a counter-ECCD component on axis.

This paper is organized as follows. Section 2 contains a brief description of the TCV tokamak and of the ECH/ECCD system, accompanied by an overview of recent results. Studies of fully non-inductive discharges with co-ECCD are discussed in section 3. In section 4 an account of our confinement studies is given, followed by concluding remarks in section 5.

2. Experimental setup and overview of ECH studies

The TCV tokamak is a medium-sized device, with major radius R=0.88 m, minor radius a=0.25 m and a maximum vacuum magnetic field B_ϕ=1.43 T; plasma currents up to 1 MA have been achieved. The highly elongated vacuum vessel is a distinguishing feature of TCV and is designed to accommodate a wide variety of plasma shapes [5]: elongations up to 2.70 and triangularities between -0.7 and +0.9 have already been achieved.

The second harmonic, X-mode (X2) ECH system comprises six gyrotrons with a 2 s pulse capability, each connected to a matching optics unit (MOU) for coupling into an evacuated waveguide; the MOU also houses a universal polarizer, which allows the selection of the appropriate X-mode polarization for each launching configuration. The power rating of each gyrotron-MOU unit is 0.47 MW. At the end of each waveguide is a launcher with two rotational degrees of freedom to provide maximum flexibility in the aiming of the injected beam. The poloidal angle can be varied in the course of a plasma discharge, while the toroidal angle can be adjusted between discharges. The average power delivered to the plasma by each launcher is 0.45 MW at a frequency of 82.7 GHz [6].

Ultimately, three additional gyrotrons at the third harmonic (X3) frequency (118 GHz) will supplement the X2 system, for a total ECH power delivered to the plasma in excess of 4 MW. The X3 waves will be launched vertically from the vessel ceiling, in a direction nearly tangential to the resonant surface in order to maximise the single-pass absorption.

ECH experiments have been carried out in TCV at progressively increasing powers during the past four years [7]. An accurate knowledge of the aiming direction and of the beam polarization is a prerequisite to studies that rely on the precise localization of the power deposition location. The behavior of the sawtooth oscillations in the plasma has been found to depend sensitively on the heating location relative to the position of the flux surface on which the safety factor q is equal to unity, as well as on the local power density and current drive component. This dependence is highly reproducible. A sweep of the poloidal injection angle of each launcher thus yields a very accurate measurement of the difference in angle between launchers, reflected in a precision of ± 3 mm in the knowledge of the relative heating location for cases in which refraction effects can be neglected. The precision on the absolute value of the angle is set by the accuracy of the magnetic equilibrium reconstruction, particularly with respect to the position of the q=1 surface. In addition, the energy content of the plasma when heating is applied inside the q=1 surface depends strongly on the beam polarization, being maximum in pure X-mode: this feature permits a verification of the correctness of the polarization [6].

Amongst the experiments performed with ECH during the past year, the exploration of H–mode accessibility at the low densities ($< 4.3 \times 10^{19}$ m^{-3}) required for X2 propagation deserves special mention. The low-density bound for the L–H transition was lowered with the addition of ECH power, from the previous limit of 3.5×10^{19} m^{-3} to 2.5×10^{19} m^{-3} in line-averaged density. Remarkably, an inverse (decreasing) dependence of the L–H threshold power on the plasma density was documented in these discharges [8].

The MHD stability properties of the plasmas in the presence of ECH have been investigated. The influence of shaping on sawteeth, previously observed in Ohmic plasmas, was significantly enhanced by central ECH: the destabilization (shortening) of sawteeth at high elongation and at low or negative triangularity is amplified by the additional heating inside the q=1 surface. Numerical analysis has shown these shapes to be unstable to the ideal internal kink. This is consistent with the lower pressure gradients measured inside the q=1 surface in these configurations [9]. Also, neoclassical tearing modes were identified

in discharges with central co-ECCD and high pressure gradients. It was also shown that a broadening of the power deposition profile inhibits the appearance of the modes, which can degrade the global confinement time by up to 25% [10].

A particle transport phenomenon, commonly known as "density pump-out", whereby particles are driven outward by intense central ECH, is observed and has been linked to MHD mode activity at the q=1 surface. Since mode stability is itself strongly dependent on shape, pump-out does not occur at high triangularity when the MHD mode activity is suppressed [11].

3. Fully non-inductive operation with electron cyclotron current drive

The plasma current in TCV has been driven entirely by co-ECCD, in steady state, with injected powers ranging from 1.35 to 2.7 MW. The highest driven current to date is 210 kA at 2.7 MW. As shown in Fig. 1, the current is sustained for the entire 2 s gyrotron pulse duration, while plasma conditions stabilize over a characteristic time scale of less than 500 ms. In the case shown, the line-averaged density is 1.3×10^{19} m^{-3} and the central temperature during ECCD is approximately 5 keV. The internal inductance is increased by ECCD, indicating a peaking of the current profile. The bootstrap current fraction, calculated by means of the finite collisionality model of Sauter et al. [12], was 8% in this discharge.

The non-inductive condition is evidenced both by the edge loop voltage averaging zero and, in steady-state conditions, by the current in the primary circuit of the Ohmic transformer remaining constant. The latter is in fact the more sensitive and less noisy of the two measurements. In normal tokamak operation, the current in the Ohmic coil is controlled by feedback to keep the plasma current equal to a predetermined value. In the present discharges, 50 ms after the start of the ECCD pulse the feedback configuration is switched so that the Ohmic coil current itself is maintained at a preset value while the plasma current is allowed to float; 50 ms before the end of the pulse, the regular feedback scheme is reinstated. This method guarantees that the inductively driven current component in the

plasma is strictly zero, once steady-state conditions are reached and the current in all the shaping coils is also constant.

In a preliminary study, it was found that the current drive efficiency at constant deposition radius increased with increasing toroidal injection angle [13]. Accordingly, in our non-inductive discharges the angle was chosen to be the largest compatible with full absorption, minus a safety margin of a few degrees to allow for possible variations in density and thus in beam refraction. The average angle of the six beams to the perpendicular direction is approximately 32° at the resonance location for the case shown in Fig. 1.

The linear ray tracing code TORAY [14], with the Cohen package for current drive estimation [15], has been our main modeling and predictive tool. The theoretical current drive efficiency is linearly dependent on the ratio of the electron temperature to the density, which is generally highest on axis, and is also strongly dependent on the fraction of particles that are trapped in the magnetic mirror created by the spatial inhomogeneity of the toroidal magnetic field [16]. As the distance from the magnetic axis increases, the trapped particle population increases and the efficiency decreases; in addition, this effect is stronger on the low field side than on the high field side of the axis. Thus, the efficiency is predicted to be a decreasing function of the minor radius through a combination of these effects.

We have attempted to maximise the efficiency by placing the deposition location of the beam as close to the magnetic axis as possible. However, we found experimentally that an MHD stability limit sets a minimum deposition width below which a disruption occurs before steady state can be attained. The ray trajectories for the case of Fig. 1, as well as the radial profiles of the absorbed power density and driven current density, are shown in Fig. 2. The width of the deposition profile relative to the plasma centre is the lowest stable width identified over a series of discharges with different launching configurations.

The minimum stable deposition profile width is found to increase with increasing injected power. This is consistent with both the pressure and current gradients, which can drive MHD instabilities, increasing with power at constant profile shape. As a result, the maximum global ECCD efficiency achievable appears to be a decreasing function of applied power. This

is evidenced by Fig. 3, which shows a comparison between the narrowest stable deposition profiles for the 2.7 MW case shown earlier and a case with only 1.35 MW. The latter was also a steady-state, fully non-inductive discharge, with a current of 160 kA.

The cause of the disruptive instability is not known at present. Low-frequency (<10 kHz) MHD modes are often detected by magnetic probes at the plasma boundary while the plasma conditions relax towards steady state. However, these modes generally disappear when the relaxation is complete; furthermore, no significant degradation in confinement is observed while the mode is present. When the disruption occurs, it is without any immediate precursors and over a time scale of the order of the Alfvén time, typically 50-200 μs, indicative of an ideal MHD instability. A comparison between a stable and an unstable case at 2.7 MW is shown in Fig. 4. The stable case reproduces the one shown in Fig. 1. The MHD mode can be seen in both discharges.

A paramount issue for ECCD applications is its efficiency, particularly its dependence on the deposition location through trapped particle effects. The normalized efficiency $\eta_T = I_{\rm EC} R n/(P T_e)$, where $I_{\rm EC}$ is the EC-driven current in A, R is the major radius in m, n is the plasma density in 10^{20} m^{-3}, P is the ECCD power in W and T_e is the electron temperature in keV, is an important figure of merit, which is theoretically expected to depend only on the trapped particle population and on the effective ion charge $Z_{\rm eff}$, which in this study is typically between 5 and 6 with no noticeable dependence on power (above 1.35 MW) or plasma conditions. The EC-driven current in the steady-state non-inductive mode is simply the plasma current minus the calculated bootstrap fraction, which is generally in the order of 10%. Although η_T is a local parameter, we have evaluated a global average $\langle \eta_T \rangle = I_{\rm EC} \left[\int dV \, P_{\rm abs} T_e/(Rn) \right]^{-1}$, where $P_{\rm abs}$ is the flux-surface-averaged EC power density calculated by TORAY. While only approximate, this procedure is in fact sufficiently accurate for our immediate purposes: owing to the observed flatness of the density profile, the variation in the quantity $T_e/(Rn)$ is mostly due to temperature variations and is typically less than 30% over the region in which 95% of the power is absorbed. By contrast, by varying the deposition profile a variation of $\langle \eta_T \rangle$ by up to a factor of $\sim$3.5 (between 1.7×10^{-3} and

6.0×10^{-3}) has been recorded, as shown in Fig. 5. Here, the deposition is generally slightly on the low field side of the magnetic axis and vertically displaced from the midplane. These preliminary results already constitute clear evidence of the dependence on the minor radius expected from trapped particle effects. In addition, we find excellent quantitative agreement, to within 20%, with the efficiencies predicted by TORAY. Thus nonlinear effects do not appear to be significant in the present conditions. It should be noted that in this comparison the spatial averaging plays no role, as the ratio between the experimental and theoretical values is simply the ratio between the respective values of the total driven current.

4. Plasma confinement properties in the presence of ECH and ECCD

Degradation of the plasma energy confinement with the application of additional heating (L–mode) is a well-established phenomenon in tokamaks. In hot electron scenarios, i.e., when heating of the electrons dominates over ion heating, the energy confinement time is generally well reproduced by the Rebut-Lallia-Watkins (RLW) scaling law [17]. In TCV, the RLW scaling appears to constitute an especially appropriate benchmark since it is in excellent agreement with experimental measurements in Ohmic plasmas and in many instances of L–mode plasmas with ECH [7]. However, in the ECCD experiments described in the previous section, as well as in numerous discharges with pure ECH, we have measured confinement times higher than the RLW scaling by a factor of two or more.

In addition, by applying counter-ECCD on axis, the confinement time is increased further with respect to cases with co-ECCD or pure ECH by up to a factor of two. Steady-state central temperatures in excess of 10 keV have been measured, and the core electron energy diffusivity is close to or lower than Ohmic levels [3]. By driving a negative current on axis, the local current density is decreased: this effect is in competition with the tendency of the current to increase owing to the rising conductivity of the heated plasma core. The first effect dominates for sufficiently large parallel wave numbers and the safety factor remains above unity. Sawtooth oscillations, which are present in co-ECCD and ECH discharges,

therefore do not develop in this case. The transport and equilibrium code PRETOR [18] is capable of reproducing the increase in confinement, indicating that the absence of sawtooth activity may be sufficient to explain this effect. This conclusion is further corroborated by the observation that if sawtooth activity is artificially suppressed in PRETOR in the co-ECCD and ECH cases, the calculated diffusivity decreases dramatically and becomes comparable to that of the counter-ECCD discharges. It is interesting to note that PRETOR itself is based on the RLW local prescription for the diffusion coefficients; however, the global scaling obtained differs from the RLW global scaling, since the calculated profiles depart from the canonical ones on which the global scaling is based. An example of this phenomenon is shown in Fig. 6. Here, an ECCD power ramp from 2 to 2.3 MW was effected; the confinement enhancement factor $H_{RLW} = \tau_{eE}/\tau_{RLW}$ is seen to increase with increasing power. This type of discharge is not always stable and in some cases the confinement is suddenly degraded at a later time or a disruptive instability occurs [4], as in the case shown in Fig. 6. The core temperature in the high-confinement phase exceeds 10 keV, as evidenced further by Fig. 7.

Similar or slightly higher confinement enhancement factors have been obtained through a specific dynamical sequence of heating scenarios [4]. First, co-ECCD or ECH is applied off axis; since the total current is kept constant, the current driven off axis (by direct drive with ECCD or by conductivity enhancement with ECH) forces the central current to decrease, engendering a similar effect to the on-axis counter-ECCD case and thus keeping the $q < 1$ region very small or inhibiting sawteeth altogether. The core diffusivity is reduced in this phase. On this baseline of high core confinement, central counter-ECCD is further added after a delay of approximately 300 ms. This sequence is shown in Fig. 8 with the high H_{RLW} factor of 4 attained in the second phase. A case with the two heating schemes applied at the same time is shown here for comparison. The confinement is initially high in this case also, but is later degraded before a steady state can be reached. This suggests that the temporal dynamics of the discharge evolution plays a crucial role in sustaining the enhanced confinement state in a stable manner. A comparison discharge was run with the same time sequence but with the on-axis beams switched to pure ECH mode, and the confinement time

was found to be significantly lower, as shown in Fig. 8. Note that in all cases $H_{\mathrm{RLW}} = 1$ in the initial Ohmic phase.

This time-delayed scenario could not be reproduced successfully by PRETOR; in particular, the temperature profiles predicted by the numerical simulation were narrower, while the peak temperature was similar. It should be noted that while the technique described generates a confinement similar to that of the purely on-axis counter-ECCD scenario, the stability properties of the former are better, presumably owing to the broader overall power deposition profile. On-axis counter current drive appears to be an essential ingredient in all the enhanced confinement regimes observed in this study.

5. Conclusions

Experiments with steady-state, fully non-inductive ECCD have progressed in TCV from an initial driven current of 123 kA with 1.35 MW to a present highest value of 210 kA with 2.7 MW. The global ECCD efficiency is found to agree well with theoretical predictions from linear modeling, including trapped particle effects, over a broad range of values: in particular, a predicted threefold decrease of the normalized efficiency with increasing deposition width was experimentally verified. MHD stability requirements are empirically found to set a lower limit on the width of the deposition profile and thus an upper limit on the normalized efficiency; the latter decreases with increasing power.

Enhanced electron energy confinement, with central diffusivity of the order of its Ohmic counterpart, is obtained with counter-ECCD on axis, owing to prevention of sawteeth. However, the confinement already exceeds the reference Rebut-Lallia-Watkins scaling by a factor of two in many sawtoothing discharges with ECH and co-ECCD, primarily as a result of peaked deposition profiles. Improved confinement is also achieved in a more MHD-quiescent configuration by a time-delayed combination of off-axis ECH or co-ECCD and on-axis counter-ECCD.

Acknowledgments

This work was supported in part by the Swiss National Science Foundation.

REFERENCES

[1] Lloyd B 1998 *Plasma Phys. Control. Fusion* **40** A119

[2] Sauter O *et al* 2000 *Phys. Rev. Letters* **84** 3322

[3] Pietrzyk Z A *et al* 2000 *Phys. Plasmas* (to be published)

[4] Pietrzyk Z A *et al* 2000 *Proc. 27th EPS Conf. on Controlled Fusion and Plasma Physics (Budapest 2000)* (to be published)

[5] Hofmann F *et al* 1994 *Plasma Phys. Control. Fusion* **36** B277

[6] Henderson M A 1999 CRPP-EPFL Report LRP 643/99 and *Proc. Fourth International Workshop on Strong Microwaves in Plasmas (Nizhny Novgorod 1999)* (to be published)

[7] Pochelon A *et al* 1999 *Nucl. Fusion* **39** 1807

[8] Martin Y *et al* 1999 *Proc. 26th EPS Conf. on Controlled Fusion and Plasma Physics (Maastricht 1999), Europhys. Conf. Abstr.* **23J** 1105

[9] Reimerdes H *et al* 2000 *Plasma Phys. Control. Fusion* **42** 629

[10] Reimerdes H *et al* 2000 *Proc. 27th EPS Conf. on Controlled Fusion and Plasma Physics (Budapest 2000)* (to be published)

[11] Furno I and Weisen H 2000 *Proc. 27th EPS Conf. on Controlled Fusion and Plasma Physics (Budapest 2000)* (to be published)

[12] Sauter O *et al* 1999 *Phys. Plasmas* **6** 2834

[13] Sauter O *et al* 1999 CRPP-EPFL Report LRP 646/99 and *Proc. IAEA Technical Committee Meeting on ECRH Physics and Technology for Fusion Devices and EC-11 (Oharai 1999), Fusion engineering and design* (to be published)

[14] Kritz A H *et al* 1982 *Proc. 3rd Varenna-Grenoble Int. Symposium on Heating in Toroidal Plasmas (Grenoble 1982)* (Brussels: CEC) Vol. II, p 707

[15] Cohen R H 1987 *Phys. Fluids* **30** 2442

[16] Alikaev V V and Parail V V 1991 *Plasma Phys. Control. Fusion* **33** 1639

[17] Rebut P H, Lallia P P and Watkins M L 1989 *Proc. 12th Int. Conf. on Plasma Physics and Controlled Nuclear Fusion Research (Nice 1988)* (Vienna: IAEA) Vol. II, p 191

[18] Boucher D and Rebut P H 1992 *Proc. IAEA Tech. Conf. on Advances in Simulation and Models of Thermonuclear Plasmas (Montreal 1992)*; Angioni C, Boucher D, Moret J-M and Sauter O 1998 *Theory of Fusion Plasmas* (Bologna: Editrice Compositori) p 493

FIGURES

FIG. 1. Steady-state, fully non-inductive 210 kA discharge with 2.7 MW of distributed co-ECCD: (a) plasma current, (b) injected electron cyclotron power, (c) loop voltage at plasma boundary, (d) current in the Ohmic transformer primary, (e) line-averaged density, (f) peak temperature, (g) internal inductance.

FIG. 2. Flux-surface-averaged (a) absorbed power and (b) driven current density as functions of a normalized radial coordinate proportional to the square root of the plasma volume, for the discharge shown in Fig. 1 at time = 2.4 s; (c) poloidal and (d) toroidal cross sections of TCV with launching geometry. All data are from TORAY. In (c) and (d) the dashed vertical line is the nominal resonance surface; the lighter ray segments denote the region of 99% absorption. The average angle between the EC rays and the magnetic field at the resonance is 32°.

FIG. 3. (a) Absorbed power and (b) driven current density for non-inductive discharge at 160 kA and 1.35 MW power ($n_{e,av} = 1 \times 10^{19}$ m^{-3}, $T_{e0} = 3.1$ keV); (c) absorbed power and (d) driven current density for non-inductive discharge at 210 kA and 2.7 MW power ($n_{e,av} = 1.2 \times 10^{19}$ m^{-3}, $T_{e0} = 3.7$ keV). All the profiles are calculated by TORAY.

FIG. 4. Comparison between (a) an unstable and (b) a stable discharge, both non-inductively driven. At the top are the driven current density profiles as given by TORAY. The time traces show, from top to bottom, the plasma current, the injected EC power and the rms value of the magnetic field fluctuations at the inner edge in the range 0-15 kHz.

FIG. 5. Profiles of normalized power density calculated by TORAY for four different discharges; from top to bottom the deposition becomes increasingly central. Experimental and theoretical (from TORAY) values of the normalized current drive efficiency $\langle \eta_T \rangle$ are given in units 10^{20} m^{-3} A m W^{-1} keV^{-1}.

FIG. 6. Discharge with counter-ECCD applied on the magnetic axis: (a) injected EC power, (b) peak temperature, (c) energy confinement time, (d) energy confinement time normalized to the Rebut-Lallia-Watkins scaling.

FIG. 7. Electron temperature profile measured by Thomson scattering along a vertical chord, for the discharge shown in Fig. 6, at time = 0.85 s.

FIG. 8. Comparisons of (a) injected EC power and (b) energy confinement time normalized to the Rebut-Lallia-Watkins scaling, in three different discharges. Circles and solid line: off-axis ECH from 0.4 s followed by on-axis counter-ECCD at 0.7 s; crosses and dashed line: off-axis ECH and on-axis counter-ECCD from 0.4 s; diamonds and dash-dot line: off-axis ECH from 0.4 s followed by on-axis ECH at 0.7 s.

Fig. 1

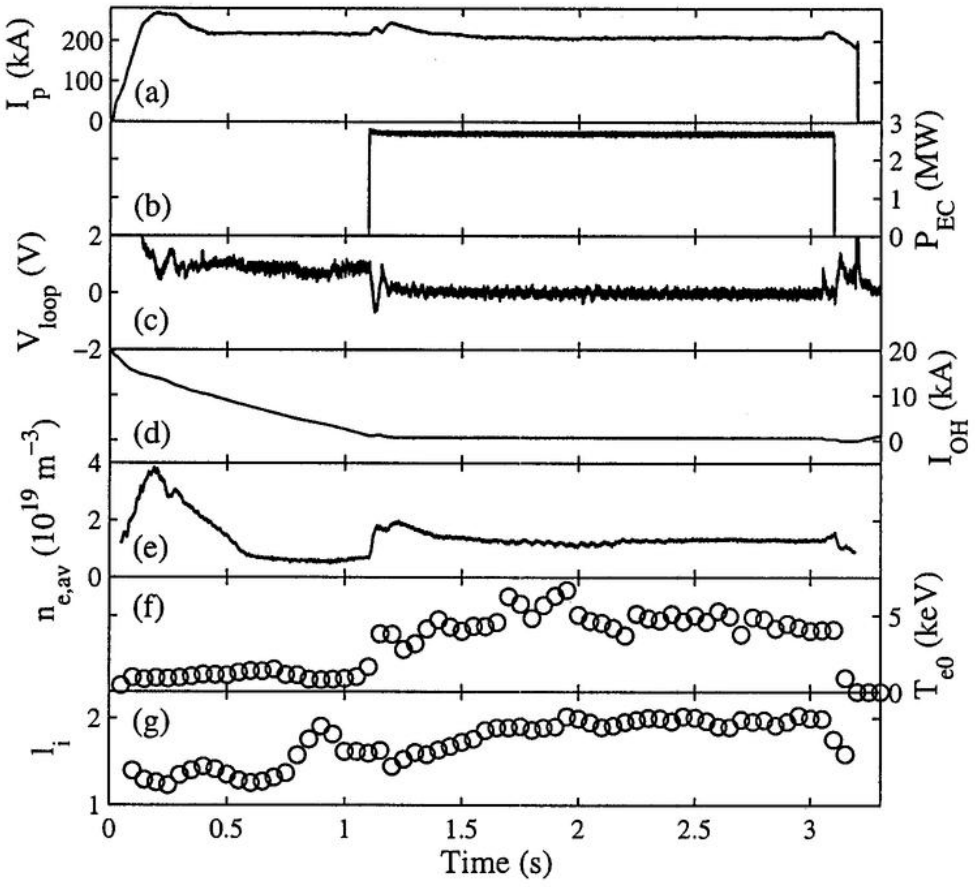
I_p (kA)
200
100
0
(a)
(b)
P_EC (MW)
3
2
1
0
V_loop (V)
2
0
−2
(c)
(d)
I_OH (kA)
20
10
0
n_e,av (10^19 m^−3)
4
2
0
(e)
(f)
T_e0 (keV)
5
0
l_i
2
1
(g)
0
0.5
1
1.5
2
2.5
3
Time (s)

Fig. 2

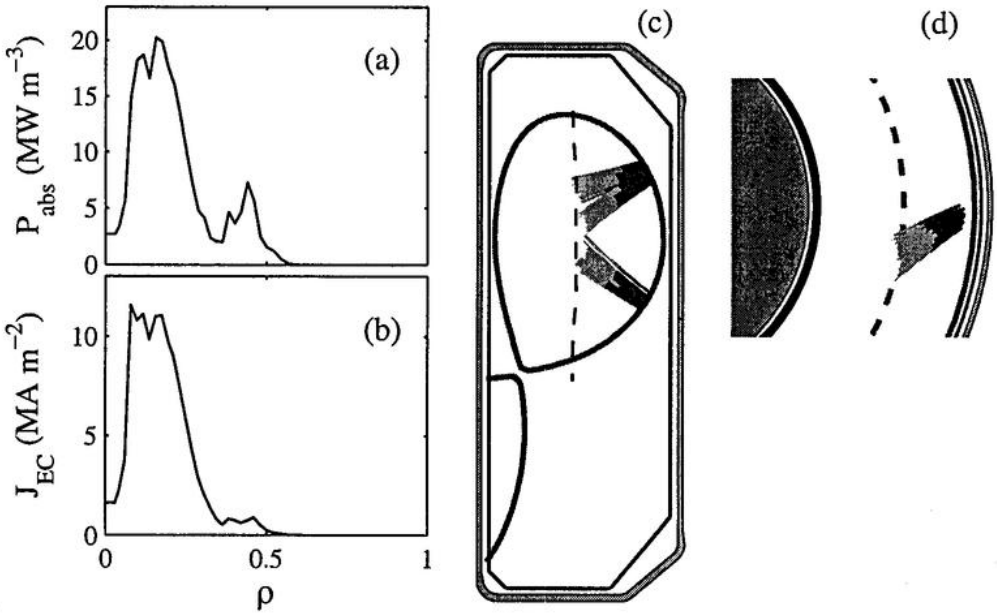

Fig. 3

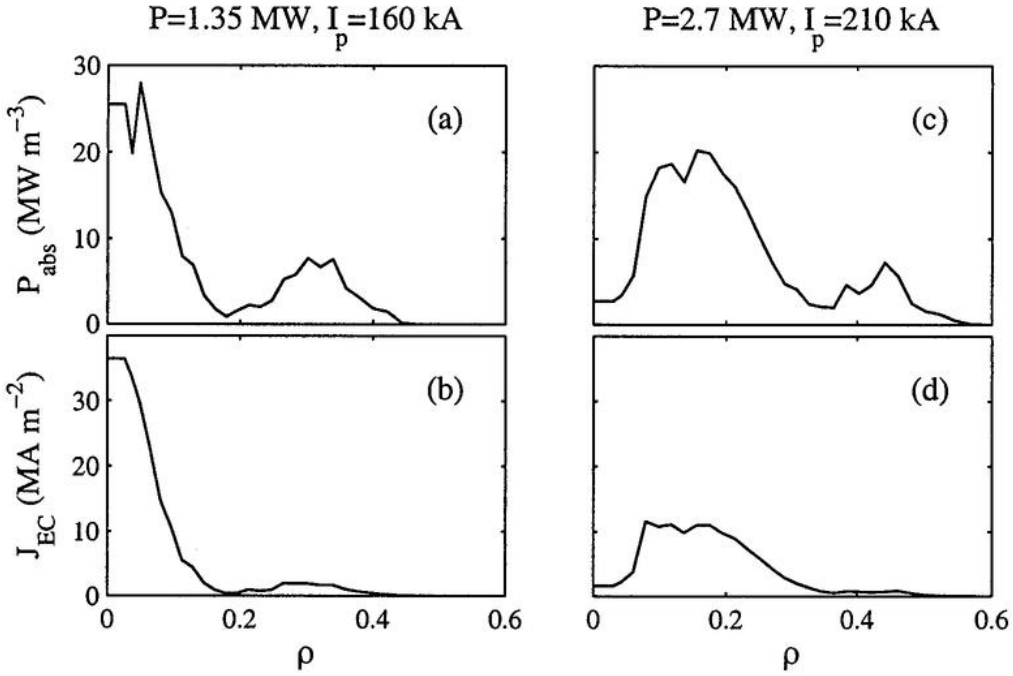
P=1.35 MW, I_p=160 kA
P=2.7 MW, I_p=210 kA
P_abs (MW m^-3)
J_EC (MA m^-2)
(a)
(b)
(c)
(d)
30
20
10
0
0
0.2
0.4
0.6
ρ

Fig. 4

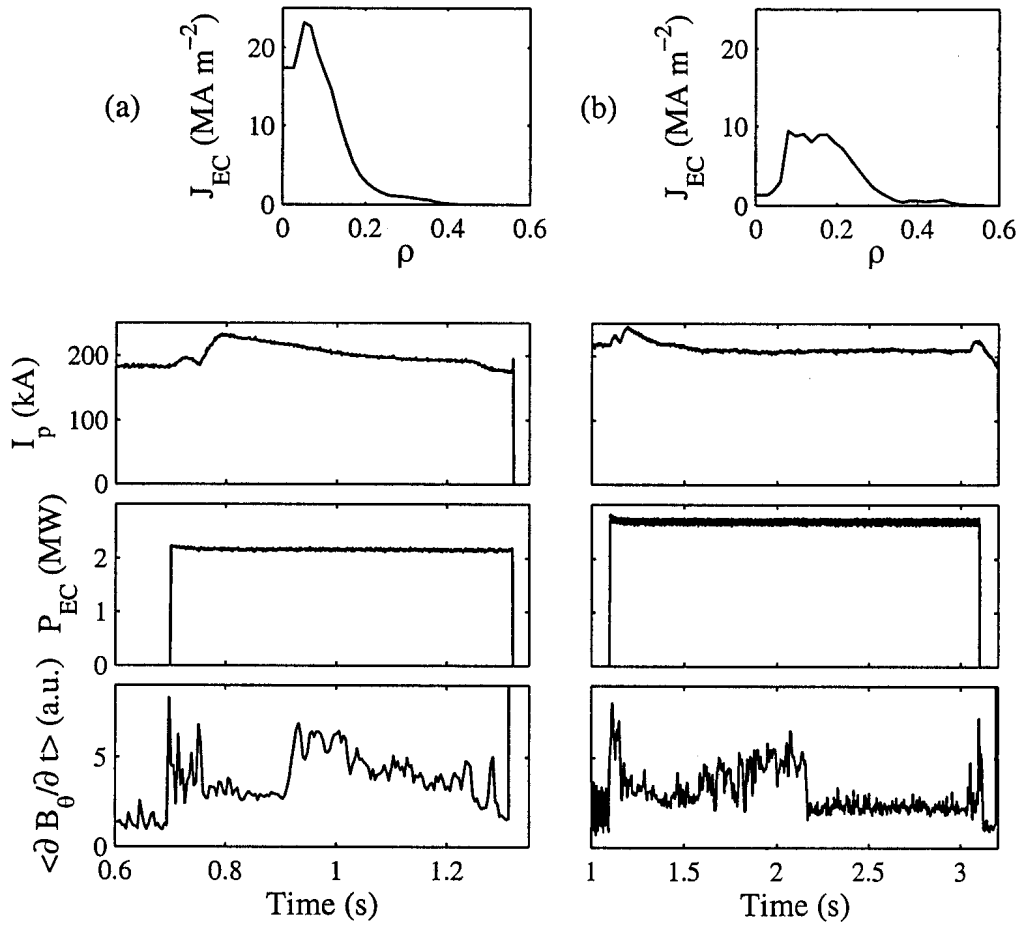
(a)
(b)
J_{EC} (MA m^{-2})
20
10
0
0
0.2
0.4
0.6
ρ
I_p (kA)
200
100
0
P_{EC} (MW)
2
1
0
<∂ B_θ/∂ t> (a.u.)
5
0
0.6
0.8
1
1.2
1
1.5
2
2.5
3
Time (s)
Time (s)

Fig. 5

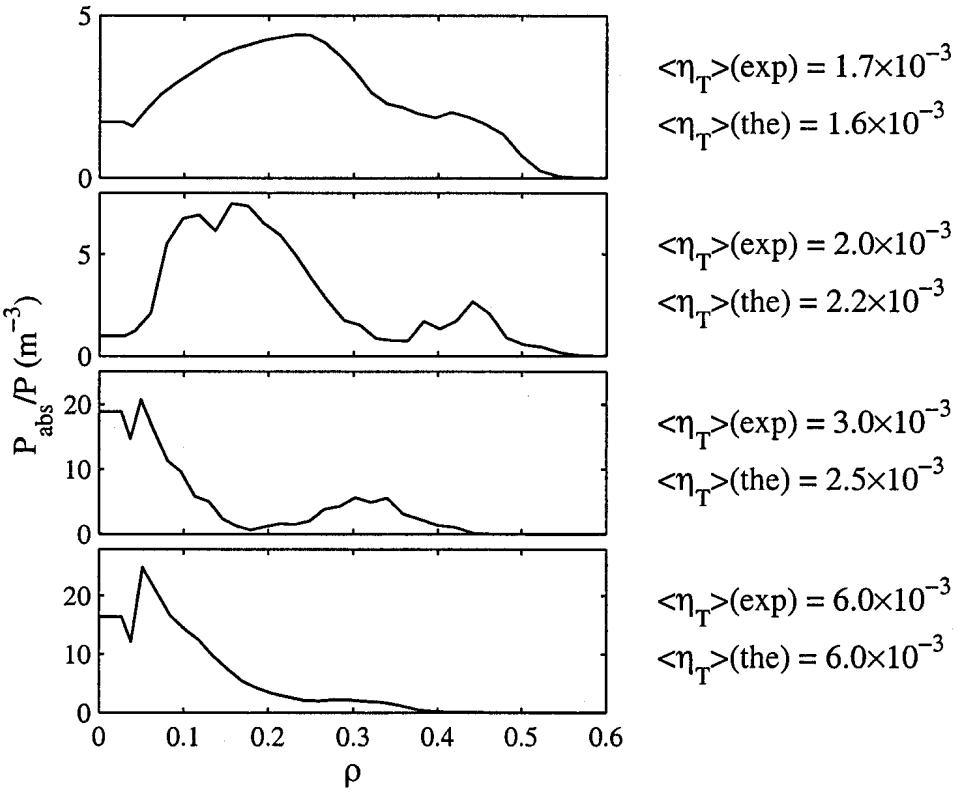
5
0
5
0
20
10
0
20
10
0
0
0.1
0.2
0.3
0.4
0.5
0.6
ρ
P_abs/P (m^-3)
<η_T>(exp) = 1.7×10^-3
<η_T>(the) = 1.6×10^-3
<η_T>(exp) = 2.0×10^-3
<η_T>(the) = 2.2×10^-3
<η_T>(exp) = 3.0×10^-3
<η_T>(the) = 2.5×10^-3
<η_T>(exp) = 6.0×10^-3
<η_T>(the) = 6.0×10^-3

Fig. 6

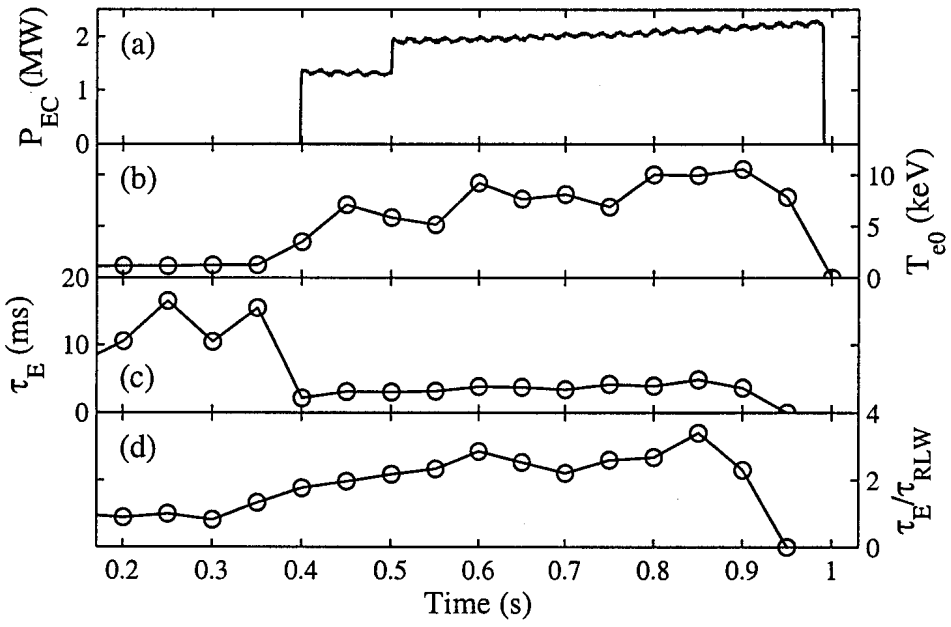
(a)
(b)
(c)
(d)
P_{EC} (MW)
T_{e0} (keV)
τ_E (ms)
τ_E/τ_{RLW}
Time (s)
0.2
0.3
0.4
0.5
0.6
0.7
0.8
0.9
1

Fig. 7

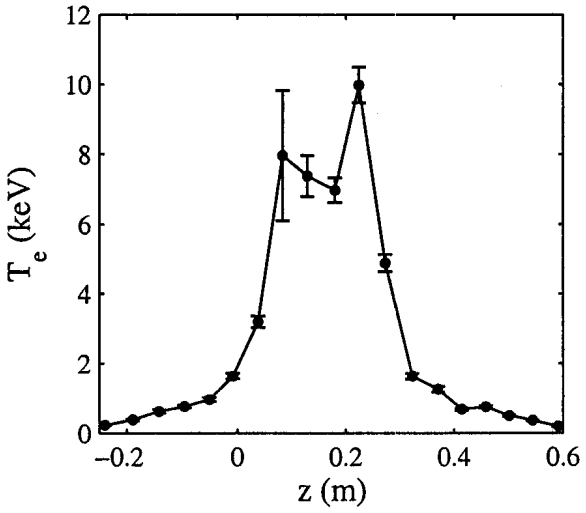

Fig. 8

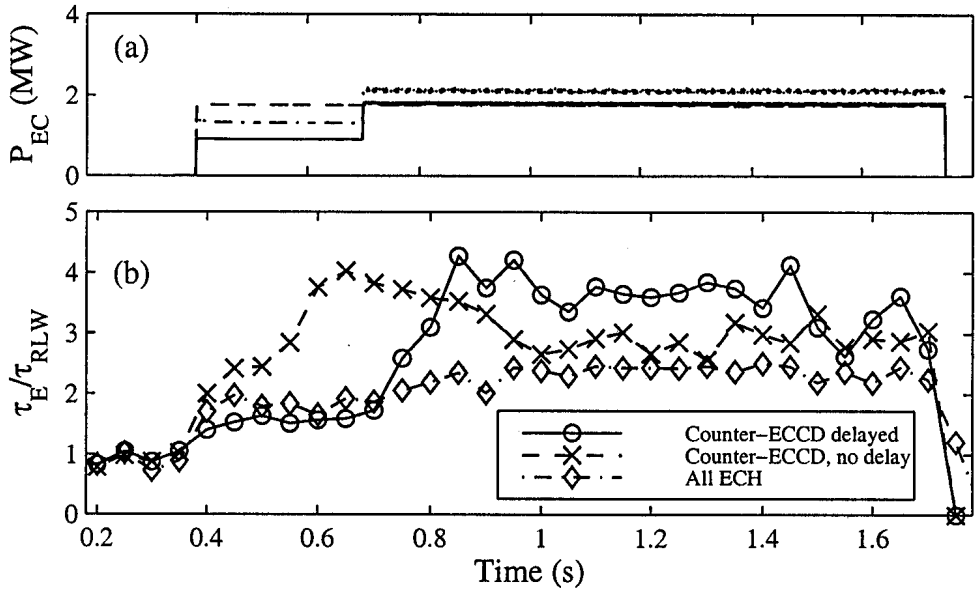
(a)
P_{EC} (MW)
4
2
0
(b)
τ_E/τ_{RLW}
5
4
3
2
1
0
0.2
0.4
0.6
0.8
1
1.2
1.4
1.6
Time (s)
Counter-ECCD delayed
Counter-ECCD, no delay
All ECH

Influence of Electron Cyclotron Heating on Electron Density Behaviour

I. Furno and H. Weisen
Centre de Recherches en Physique des Plasmas
Association EURATOM - Confédération Suisse
Ecole Polytechnique Fédérale de Lausanne, CH-1015 Lausanne, Switzerland

SUMMARY

Understanding the coupling between heat and particle transport in tokamak plasmas with elongated and shaped cross-sections is essential for fusion devices. A consequence of the coupling between heat and particle transport is the drop of the central line integrated density, $\bar{n}_e$, (pump-out) which is observed during Electron Cyclotron Heating (ECH) in many tokamak experiments [1]. Despite the importance of this effect, there is little understanding of the underlying physical phenomena.

On TCV (Tokamak à Configuration Variable, R = 0.88 m, a = 0.25 m, vacuum vessel elongation κ = 3 and vacuum central magnetic field $B \leq 1.43$ T) a series of experiments has been carried out to investigate the electron density pump-out in sawtoothing plasma discharges under intense localised ECH. The steerability of the ECH launching system and the capability of TCV to produce a large variety of plasma shapes have allowed a detailed study of the pump-out under different heating scenarios. For these experiments, TCV was operated with up to six 82.7GHz, 500kW gyrotrons, with a 2s pulse length, for heating at the second cyclotron harmonic resonance (X2-mode). The 6 launching mirrors are separately orientable in the toroidal and poloidal direction. The vertical microwave beam width near the plasma centre is $w \approx 2.5$ cm in free-space (beam intensity $\propto exp[-2(r/w)^2]$, where r is the distance transverse to the direction of the beam propagation). Local ECH power densities in excess of 10MW/m^3 have been obtained.

These experiments showed that in sawtoothing discharges the electron density response to heating conditions is dependent both on the plasma shape and the injected power, P_{ECH}. In low triangularity plasmas for central ECH and ECCD, particles are expelled from the plasma core during the sawtooth reheating phase resulting in a flattening of the electron density profile. This phenomenon produces inverted sawteeth [2] and is accompanied by strong $m/n = 1$ mode activity. Hollow electron density profiles are sustained during the whole sawtooth cycle in the ECCD case. The particle outflux is terminated by the sawtooth crash, during which the central electron density rapidly recovers. The relative amplitude of the recovery strongly depends both on plasma shape and heating conditions, increasing with injected power and decreasing with the plasma triangularity. At high triangularity, no pump-out and no mode activity are observed during the sawtooth reheat phase.

The correlation between pump-out and the presence of central mode activity suggests that the mode activity is responsible for this coupled transport phenomenon.

EXPERIMENTAL OBSERVATIONS

The electron density and the sawtooth shape response to a sweep of the EC injection angle is shown in Fig. 1. In what follows, the plasma parameters are taken at the Last Close Flux Surface and in the present case are: δ_a = 0.18, κ_a = 1.3, I_P = 193 kA, q_a = 4.55, P_{ECH} = 500 kW. The EC power absorption location is scanned through the plasma along the vertical resonance position for the X2-mode (Fig. 1a) at a velocity of 3.5cm / 100ms. The plasma shape remains constant, albeit with a varying incidence poloidal angle, ϑ, and beam

width. The time behaviour of the central line integrated electron density $\bar{n}_e$ depends on the ECH power deposition location. The interval [A,B] highlighted in yellow in Fig. 1e, corresponds, within the experimental uncertainties, to power deposition inside the sawtooth inversion surface as determined from the tomographic inversion of soft X-ray measurements. For injection angles outside the interval [A,B], $\bar{n}_e$ increases during the sawtooth ramp and then drops at the crash on a fast time scale (typically $\tau_{crash} < 100\,\mu s$), Fig. 1g. The relative crash amplitude is $\Delta\bar{n}_e/\langle\bar{n}_e\rangle \sim -1\,\%$, where the brackets $\langle\ \rangle$ indicate the average of a quantity evaluated before and after the sawtooth crash (see Fig. 1g). During the sawtooth ramp, the soft X-ray emissivity is poloidally symmetric with no detectable MHD mode activity. At the sawtooth crash, $m/n = 1/1$ precursor oscillations are seen ~100μs before the sawtooth crash, Fig. 1f.

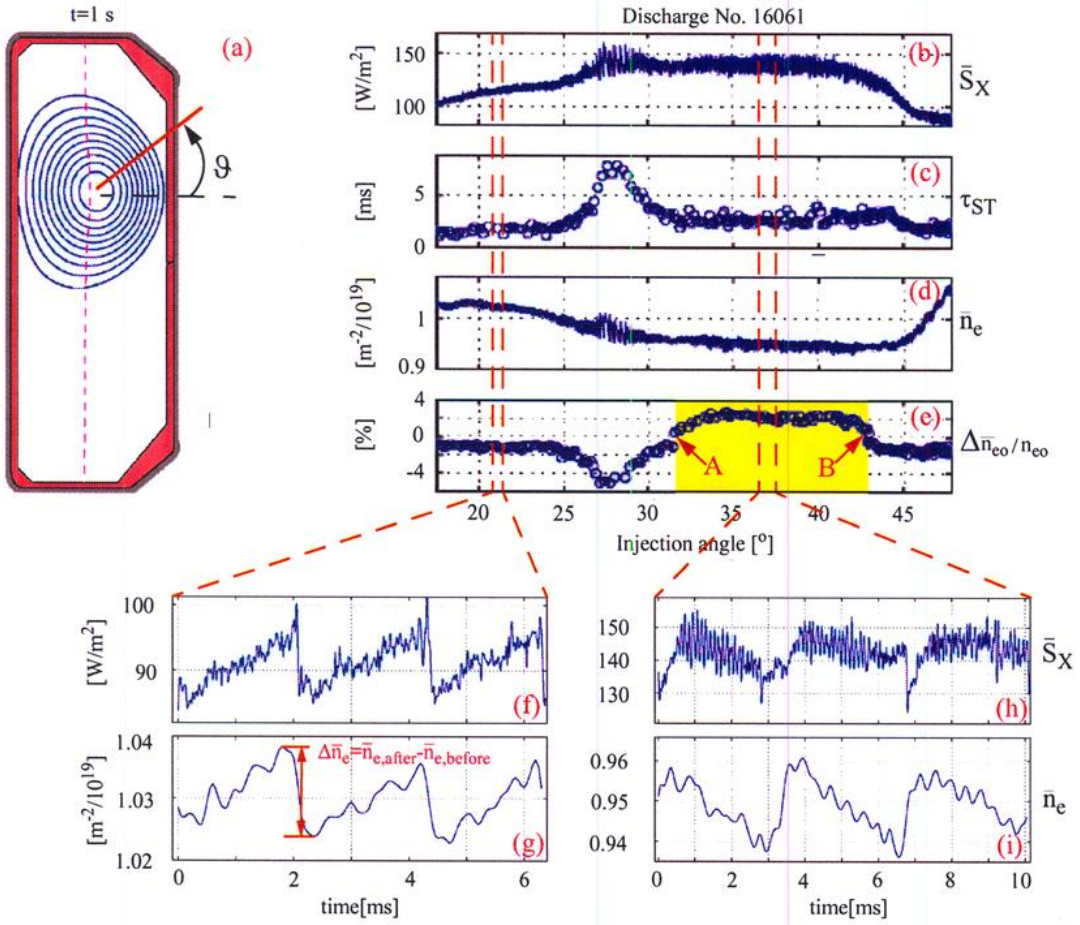

Fig. 1 Top: (a) Poloidal cross section of the plasma. The absorption layer for the X2-mode and the ECH launching geometry are shown. (b) Central line integrated soft X-ray signal. (c) Sawtooth period. (d) Central line integrated density. (e) Relative variation of $\overline{n_{e0}}$ at the sawtooth crash. Bottom: two types of sawtooth shapes from a central line integrated soft X-ray channel (f, h) and from a central line integrated electron density (g, i).

When the ECH power deposition moves inside the interval [A,B], particles are expelled from the plasma centre during the reheat phase, resulting in inverted sawteeth on the central electron density, Fig. 1i. The central soft X-ray emissivity remains almost constant or even decreases until the following sawtooth crash, Fig. 1h. This saturated phase is accompanied by a strong $m/n = 1$ mode rotating in the electron diamagnetic drift direction. The particle outflux is terminated by the sawtooth crash, during which the electron density rapidly

recovers (typically $\tau_{recover} \sim \tau_{crash}$). The relative amplitude of the recovery, $\Delta\bar{n}_e/\langle\bar{n}_e\rangle = 2\,\%$, is approximately constant for injection angles inside the interval [A,B].
The dependence of sawtooth behaviour on the injected ECH power is presented in Fig. 2. The temporal evolution of the central electron density n_{e0} from Abel-inverted multichord interferometer measurements, Fig. 2(d, e, f), is shown together with the central soft X-ray emissivity, Fig. 2(g, h, i). Plasma parameters are: $\delta_a = 0.23$, $\kappa_a = 1.54$, $I_P = 393\,\mathrm{kA}$, $q_a = 2.9$. The EC resonance position is located inside the sawtooth inversion radius, Fig. 2a, and P_{ECH} is increased in three steps from 0.5MW to 1.4MW, Fig. 2b. For this plasma shape, the central ECH deposition strongly perturbs the triangular Ohmic sawteeth. With $P_{ECH} = 1.4\,\mathrm{MW}$, the sawtooth period, $\tau_{ST} \sim 3.9\,\mathrm{ms}$, is significantly longer than the Ohmic sawtooth period $\tau_{ST} \sim 2\,\mathrm{ms}$ and the n_{e0} behaviour changes from triangular (Fig. 2f) to inverted (Fig. 2i). In the inverted sawtooth case, the electron density recovery $\Delta\bar{n}_e/\langle\bar{n}_e\rangle$ increases from 1.6% at $P_{ECH} = 0.8\,\mathrm{MW}$ to 2.3% at $P_{ECH} = 1.4\,\mathrm{MW}$. During the associated inverted sawtooth ramp, the decrease in n_{e0} results from a flattening of the electron density profile and is correlated with the presence of $m/n = 1$ mode activity. With higher P_{ECH}, partial collapses of the soft X-ray emissivity are observed during the particle pump-out which result in a flattening of the soft X-ray emissivity profile.

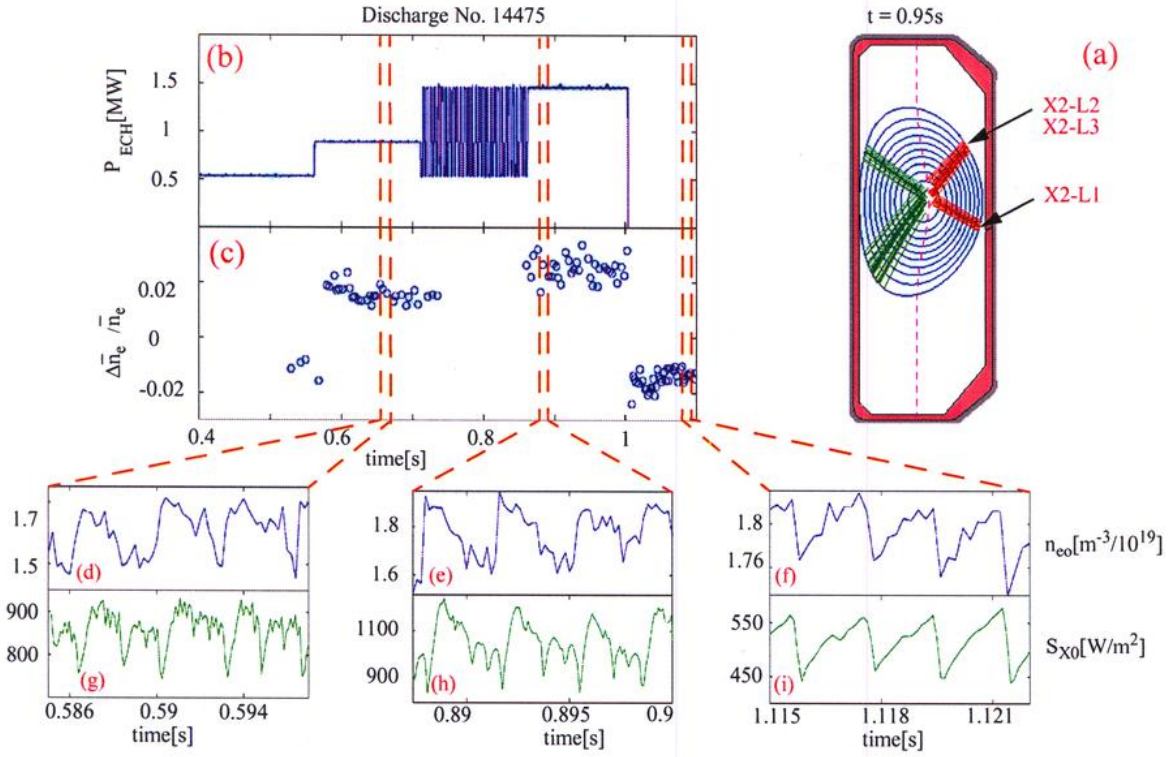

Fig. 2 Top: (a) Poloidal cross section of a plasma and ECH launching geometry for central power deposition. The absorption layer for the X2-mode and the ECH beams are indicated. (b) Stepping up of the ECH power. (c) Relative variation of $\bar{n}_e$ at sawtooth crash. Bottom: saw-tooth shapes at different injected ECH power on local soft X-ray emissivity (g, h, i) and from Abel-inverted central electron density (d, e, f).

An extreme example of electron density pump-out has been obtained in the case of full current replacement [3] with Electron Cyclotron Co-Current Drive at an injected power $P_{ECH} = 2.7\,\mathrm{MW}$. In this case, hollow electron density profiles are sustained during the whole sawtooth cycle. Figure 3 shows the electron density profile relative to a time just before the sawtooth crash where $n_e(r_{inv})/n_e(0) \sim 1.42$. At the sawtooth crash, the density recovery is

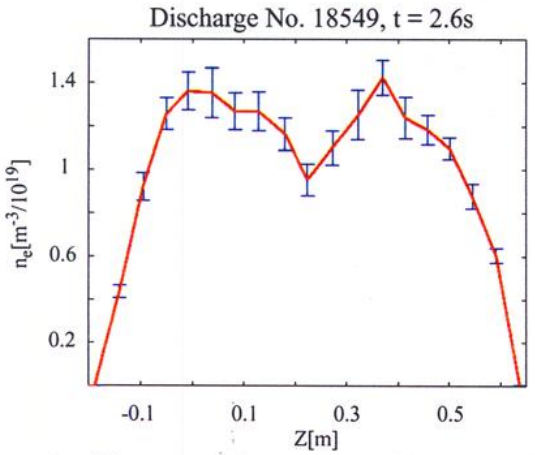

Fig. 3 Electron density profile the TCV discharge No. 18549 (I_P = 210 kA, δ_a = 0.42, κ_a = 1.62, q_a = 7.8, $n_{e0} = 9.8 \cdot 10^{18}\, m^{-3}$. The profile is relative to a time just before the central electron density recovery at the sawtooth crash.

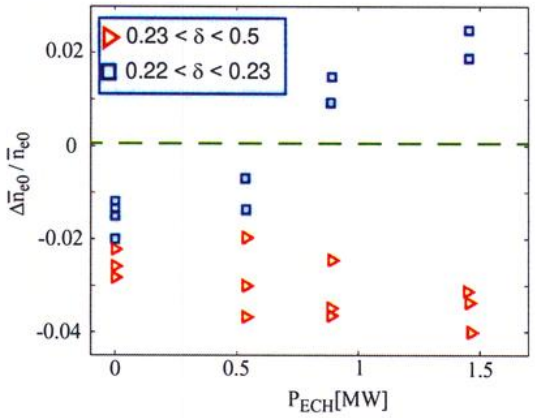

Fig. 4 Relative variation of $\bar{n}_e$ at the sawtooth crash for different plasma shape and injected ECH power. Positive and negative $\Delta\bar{n}_e/\langle\bar{n}_e\rangle$ values indicate respectively inverted and normal sawteeth.

such that $\Delta\bar{n}_e/\langle\bar{n}_e\rangle$ ~5.5% and results in flatter n_e profiles (not shown in the figure) with $n_e(r_{inv})/n_e(0) \sim 1.08$.

The effect of the plasma shape on the electron density behaviour has been studied by varying the elongation from 1.06 to 2 and the triangularity from -0.28 to 0.5. Since high elongation and low triangularity reduce the sawtooth amplitude [4] resulting in barely detectable sawteeth on the electron density, the data presented in Fig. 4 are in the following parameter range: $0.2 < \delta_a < 0.5$ and $1.02 < \kappa_a < 1.62$. In order to separate the afore mentioned dependences, the electron density, temperature and current profiles have been kept similar. The last condition was fulfilled by adjusting the average current density, in order to keep the sawtooth inversion radius constant and thus the broadness of the current profile [5]. The ECH power was increased in three steps. For all the discharges, the power deposition region was inside the sawtooth inversion surface. Figure 4 shows the dependence of $\Delta\bar{n}_e/\langle\bar{n}_e\rangle$ as a function of P_{ECH} for different plasma shapes. In strongly triangular plasmas (triangles in Fig. 4), the $\Delta\bar{n}_e/\langle\bar{n}_e\rangle$ increases from ~2%, in the Ohmic phase, to ~4% with P_{ECH} = 1.4 MW and no MHD activity is detected during the sawtooth ramp. Low triangularity plasmas (squares in Fig. 4) show normal sawteeth below $P_{ECH} \sim 0.6$ MW and inverted sawteeth above this threshold. In all this situations, the relative amplitude of the recovery increases with P_{ECH}.

Acknowledgements

This work was partly supported by the Swiss National Science Foundation.

References

[1] TFR-GROUP, Nucl. Fusion **25** (1985) 1011.
[2] Pietrzyk, Z.A., et al., Nucl. Fusion **39** (1999) 587.
[3] Coda, S., et al., invited paper T16 this conference.
[4] H. Reimerdes, et al., Plasma Phys. Control. Fusion **42** (2000) 629.
[5] H. Weisen et al., Plasma Phys. and Control. Fusion **40** (1998) 1803.

Effect of ELMs on the Measurement of Vertical Plasma Position in TCV

F. Hofmann, I. Furno, Y. Martin, H. Reimerdes

Centre de Recherches en Physique des Plasmas,
Association EURATOM - Confédération Suisse,
Ecole Polytechnique Fédérale de Lausanne, CH-1015 Lausanne, Switzerland

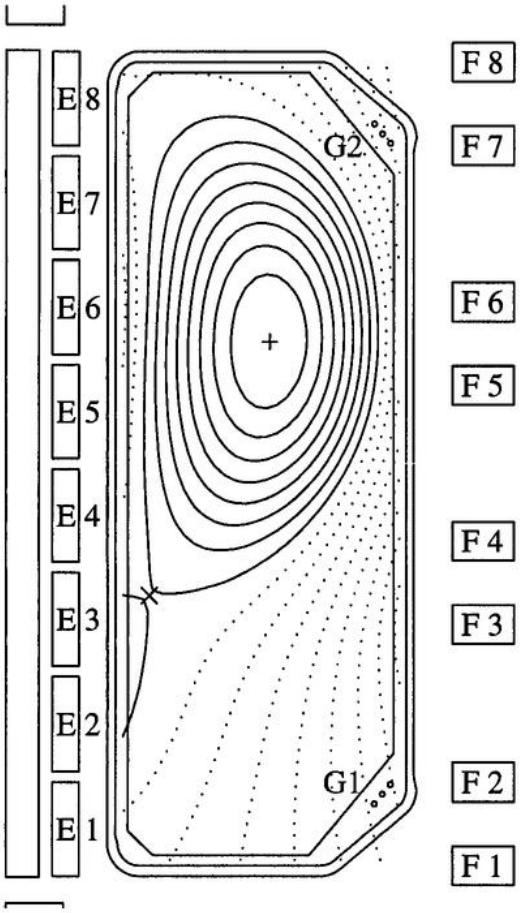

Fig.1. ELMy H-mode plasma in TCV: Shot # 18416 at 0.57 s, I_p=513kA, B_{tor}=1.45T, κ=2.03, δ=0.45, ELM frequency=170 Hz. Feedback for vertical position control is applied to coils F3, F4, F7, F8, G1 and G2.

1. Introduction

It is well known that tokamak plasmas with elongated and shaped cross-sections offer higher beta limits and better confinement than circular plasmas. This fact is the main motivation for the recent evolution of the ITER design towards higher elongation and triangularity. However, elongated cross-sections inevitably lead to vertically unstable plasmas, requiring a passive shell and active feedback coils for stabilization. One of the key elements of the feedback system in an elongated tokamak is the vertical position observer, i.e. the measurement of the vertical plasma position in real time. This measurement is usually obtained from a linear combination of magnetic field probe and flux loop signals and, consequently, it can be perturbed by plasma effects, such as sawteeth, ELMs and non-axisymmetric MHD modes, which are not necessarily related to the vertical displacement instability. Some of these perturbations, e.g. n>0 modes, can be eliminated by a judicious combination of magnetic probe arrays, located in different toroidal locations, but other effects, such as ELMs, will always interfere with the vertical position control system. In the case of large ELMs, the interference can lead to saturation of control coil voltages and currents and, subsequently, to Vertical Displacement Events (VDE's) and disruptions [1]. Several methods have been proposed to reduce or eliminate the effect of ELMs on the vertical position control system. One method consists of switching off the vertical feedback for a short time interval during each ELM. This method requires a reliable ELM detector which can be used as a trigger for switching off the feedback. It can only be used if the growth time of the vertical instability is considerably longer than the duration of a typical ELM. Another method uses an intelligent, nonlinear controller which recognizes the ELM and applies an optimized control scenario during the ELM perturbation. In this paper, we investigate the effect of ELMs on the vertical position observer in TCV and we show that a minor modification of the classical observer can greatly reduce its sensitivity to ELMs.

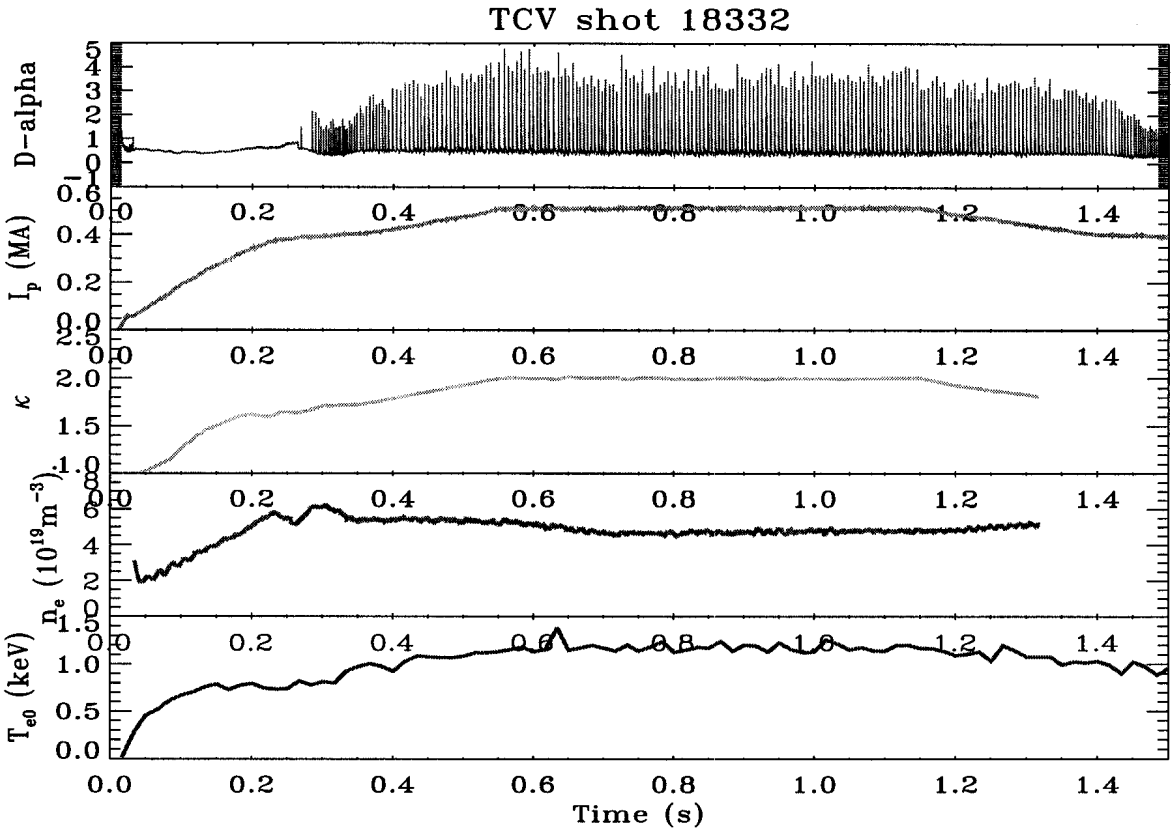

Fig.2: ELMy H-mode discharge in TCV, showing (top to bottom) D-alpha light, plasma current, elongation, line average electron density and electron temperature on axis.

2. Perturbation of the Vertical Position Control System by ELMs

TCV has a unique vertical position control system using active feedback coils both outside and inside the vacuum vessel [2]. The external coils (F-coils in Fig.1.) are driven by slow power supplies with a response time of ~1 ms, whereas the internal coils (G-coils) are driven by a fast supply with a response time of less that 0.1ms. The F-coils are used for proportional and derivative feedback and the G-coils are used exclusively for derivative feedback. The system allows the stabilization of elongated plasmas with very high growth rates and extremely low stability margins [2].

Steady-state ELMy H-mode plasmas are produced routinely in TCV [3]. Here, we consider an Ohmic, single-null divertor discharge (Figs.1 and 2), whose ion grad B drift is in the unfavourable direction, i.e. away from the X-point. Magnetic perturbations produced by ELMs can be seen mainly in the fast control loop. This loop uses a vertical position observer consisting of a linear combination of magnetic field probe signals. The probes are installed inside the vacuum vessel in several poloidal planes [4]. For vertical position control, we use the average signals of two poloidal arrays which are displaced toroidally by 180^0. The probes measure the poloidal field parallel to the vessel wall. They are distributed uniformly over the poloidal circumference and they are numbered clockwise, from 1 to 38, starting from the inboard midplane. The coefficients which are used to construct the vertical position signal are shown in Fig.3a. Note that probes 13-16 and 24-27 are not used in this observer, i.e. their coefficients are zero. This choice is motivated by the fact that these probes are located in the vicinity of the internal active coils (G1, G2) and that we wish to avoid direct coupling between the active coils and the observer.

The effect of ELMs on the observer output and hence, on the G-coil voltage, is seen in Fig.4b. Each ELM produces a perturbation of the vertical velocity signal lasting for approximately 1ms. The perturbation is significant but, in this case, it does not lead to saturation of power supply voltages or currents and hence the plasma survives.

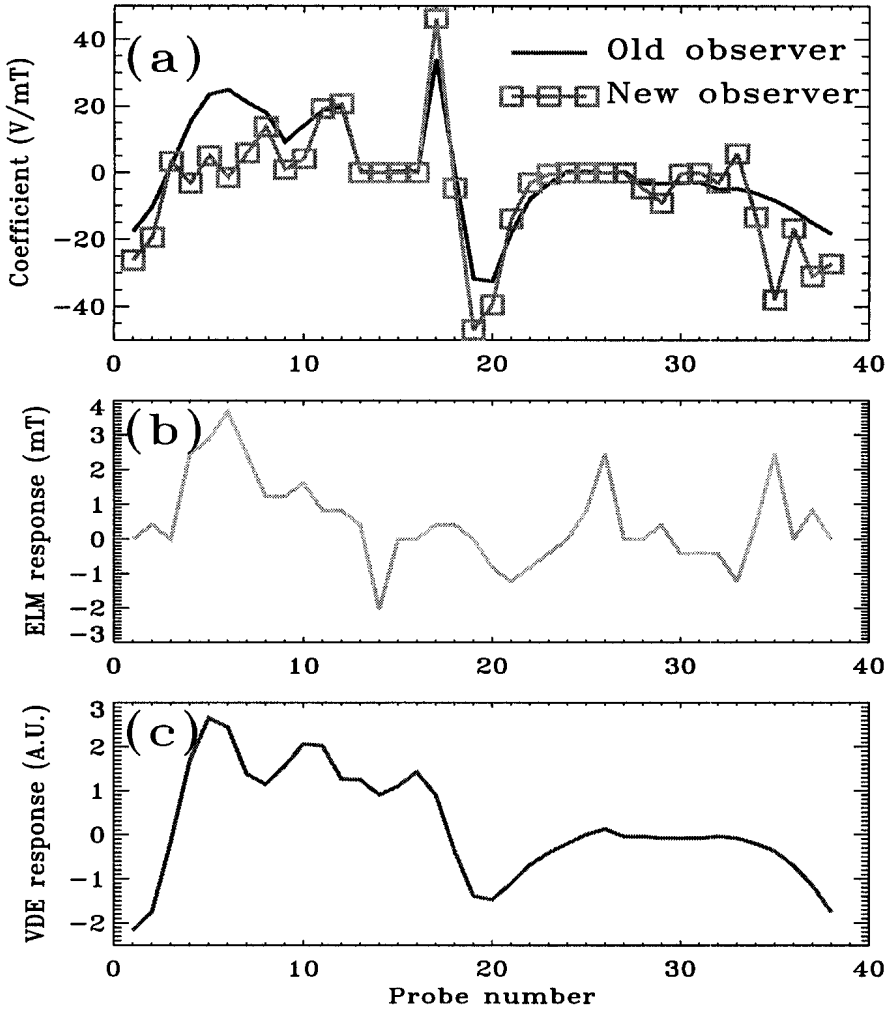

Fig.3.: (a) Old and new observer coefficients vs. probe number, (b) ELM response (Shot 18329 at 0.76s), including effect of internal active coils (peaks at #14 and #26), (c) Response of a VDE (Shot 15971 at 0.605 s). The VDE was intentionally produced by a preprogrammed feedback cut.

3. ELM and VDE Signatures

Figure 3b. shows the poloidal field perturbation produced by a typical ELM. Here, we plot the poloidal field difference between the time when the ELM perturbation reaches its maximum and the time immediately preceeding the ELM. The measurement was performed under closed loop conditions. As a result, we see both the signature of the ELM and the effect of the current pulse in the internal active coil (peaks at #14 and #26). The ELM signature can be compared with a typical VDE signature. Figure 3c. shows poloidal field measurements during a VDE which was induced by a feedback cut. We note that VDE and ELM signatures are quite different and this difference can be exploited for the construction of an ELM-resistant observer.

4. New Observer

Using the measurements presented above, we can now proceed to the construction of a new observer which satisfies the following four constraints: (1) the new observer coefficients must be orthogonal to the fast ELM response, (2) the new observer must give the same response to a rigid vertical displacement of the plasma as did the old observer, (3) the coefficients 13-16 and 24-27 must be zero to avoid coupling with the active coil and (4) the difference between the new and old observer coefficients should be minimized in the least squares sense. The result of this optimization procedure (Fig.3a.) shows that a minor modification of the observer coefficients is sufficient for satisfying the constraints mentioned above.

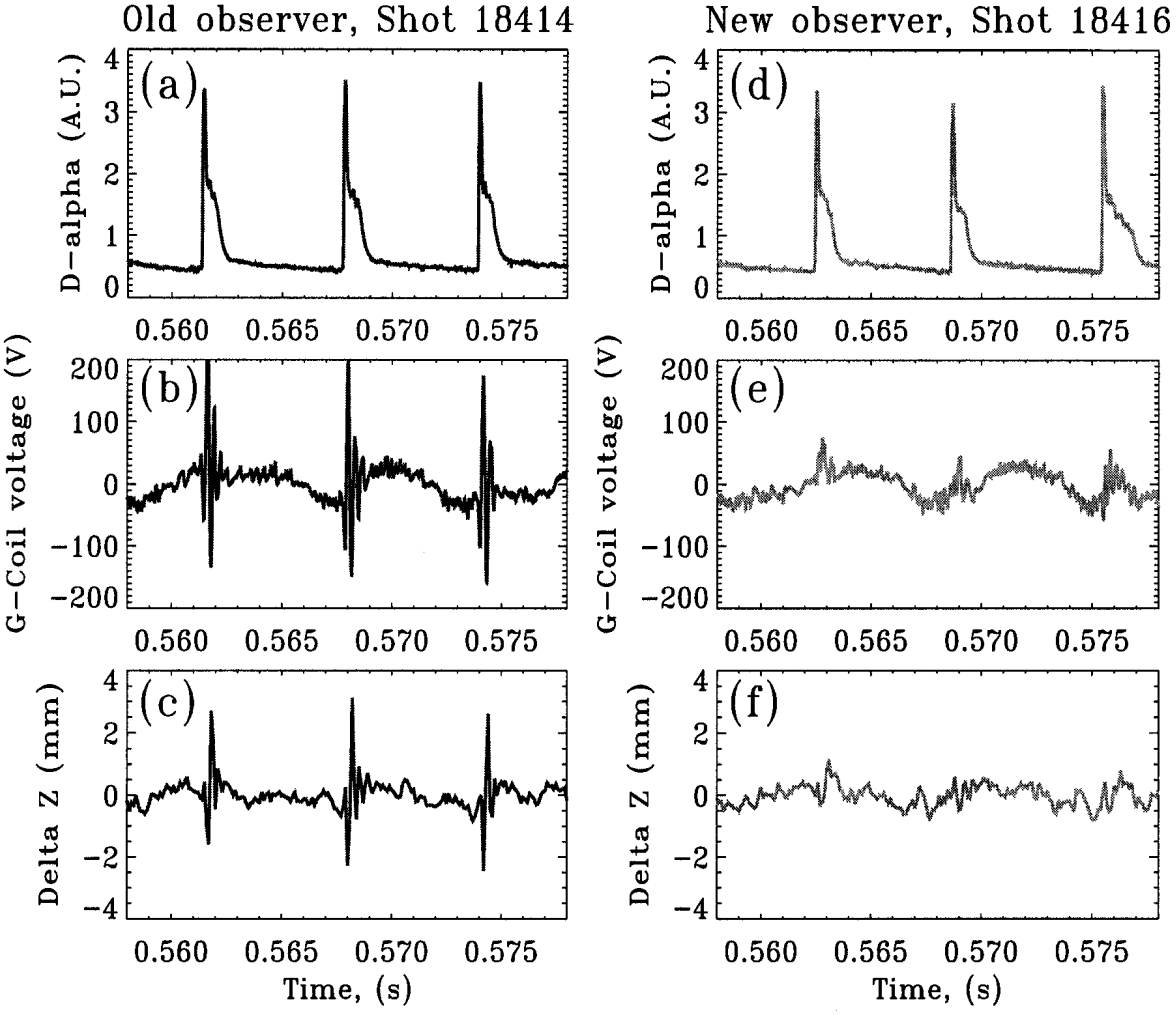

Fig.4.: (a) and (d): D-alpha signals of two identical ELMy H-mode discharges in TCV: (b) and (e): G-coil voltage, proportional to vertical plasma velocity, as obtained from old and new observers. (c) and (f): Vertical plasma displacement as obtained from LIUQE equilibrium reconstructions at 10 kHz sampling rate.

The new observer was tested in TCV by applying it to a typical steady-state ELMy H-mode plasma (Fig.2.). This plasma has relatively high elongation (κ=2) and, consequently, a high vertical instability growth rate (γ=1300 s^{-1}). ELM effects of the new and old observers are compared in Fig.4. It is seen that the new observer reduces the voltage pulses in the fast control loop by at least a factor of 5 (Figs. 4b and 4e). In addition, the vertical position excursion produced by each ELM is reduced by more than a factor of 3 (Figs. 4c and 4f). From these results we conclude that the perturbations produced by ELMs in the TCV vertical position control system can be significantly reduced by using an optimized vertical position observer.

Acknowledgements:
This work was partly supported by the "Fonds National Suisse de la Recherche Scientifique".

References:
[1] T. N. Todd et al., Plasma Phys. Control. Fusion **35** (1993) B231.
[2] F. Hofmann et al., Nucl. Fusion **38** (1998) 399.
[3] Y. Martin et al., this Conference.
[4] J.-M. Moret et al., Rev. Sci. Instrum. **69** (1998) 2333.

Plasma Equilibrium Response Modelling Experiments on the JT-60U and TCV Tokamaks

J.B. Lister[1], R. Khayrutdinov[2], D.J.N. Limebeer[5], V. Lukash[3], Y. Nakamura[4], A. Sharma[5], J.P. Wainwright[5], R. Yoshino[4]

[1]*Centre de Recherches en Physique des Plasmas, Association EURATOM-Confederation Suisse, EPFL, 1015 Lausanne, Switzerland*
[2]*Triniti, Troitsk, Russian Federation*
[3]*RRC Kurchatov Institute, Moscow, Russian Federation*
[4]*Naka Fusion Research Establishment, JAERI, Naka, Japan*
[5]*Imperial College of Science, Technology and Medecine, London, UK*

Abstract: Experimental measurements of the plasma equilibrium dynamic response to poloidal field coil voltage variations have been performed on the JT-60U tokamak. The results have been compared with the RZIP rigid current displacement model previously validated on TCV, enhanced for this work. Although such linear response models are useful for feedback controller design, their linear time-invariant properties cannot simulate the evolution of a plasma discharge. A suitable code for this purpose is DINA, benchmarked against a complete set of experimental data from TCV control experiments in both the time and frequency domains.

DINA simulations of TCV: Considerable attention is being focused on the design of plasma position, current and shape controllers for the next generation tokamak-reactor designs like ITER-FEAT. The development of a new control algorithm for a new plasma configuration will require numerical analysis prior to experimental tests to optimise experimental time. It is therefore necessary to have a validated tokamak plasma simulator to test any new proposed plasma controller design. A first requirement of such a tool is its ability to model a real experimental plasma evolution with sufficient accuracy. Considerable success had been obtained in modelling the stationary phase of TCV discharges using two linear models, RZIP and CREATE-L. However, to simulate a full discharge we require a non-linear self-consistent model. DINA is a tokamak plasma simulation code comprising a 1.5D axi-symmetric, time-dependent, resistive MHD and transport-modelling free boundary equilibrium solver in an externally imposed magnetic field and is a suitable candidate for such work. In this paper DINA is validated against an extensive set of TCV plasma equilibrium response experiments.
Initial test runs indicated that two improvements were useful. Firstly the feedback controller for these discharges has a high low-frequency gain to reduce static offset. The feedback controller had to be initialised suitably at the start of the simulation to avoid a transient which could drive the simulation unstable and even end it prematurely, Fig.1. Secondly, it is difficult to adjust the poloidal flux consumption between the experiment and the simulation, since the latter did not model the transport. Modelling the transport would not have helped since a long adjustment by trial and error would again have been necessary to obtain modest agreement. A simple solution was therefore adopted, feeding back the toroidal resistance to agree with the experiment. This adjustment did not perturb the investigation into the dynamic equilibrium response which in most cases was assessed with the lowest frequency (drift and offset) removed.
With these two improvements, a total of 27 discharges were simulated with no adjustment, with one minor numerical problem encountered for one discharge. Both limited and diverted plasmas are well modelled during the plasma current flat-top for the rejection of external square-wave PF coil voltage pulses. Examples of the comparison between TCV and DINA responses are shown in Fig.2. The agreement between the simulation and the experimental

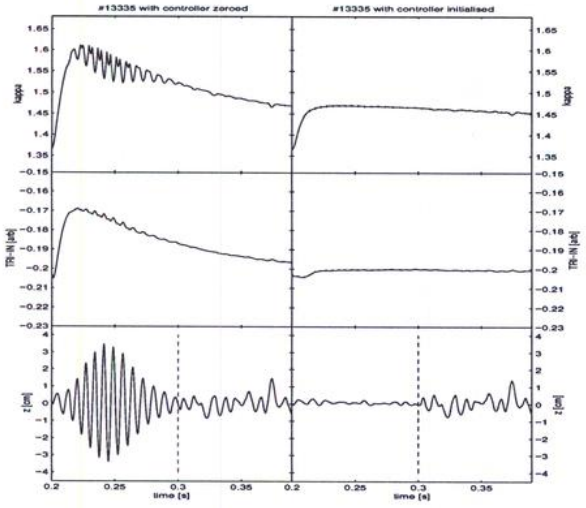

Figure 1 Improvement to the controller initialisation caused a significant reduction to the transients at the start of the DINA simulation (right). Uninitialised (left), the transient included an increase to the vertical field decay index and hence to the elongation (top trace), resulting in an anomalous vertical instability showing up on the vertical movement trace (bottom) which caused a failure of the simulation in early tests. The middle trace shows the excursion of the control parameter for elongation. The start of the stimulation is indicated as a vertical dotted line.

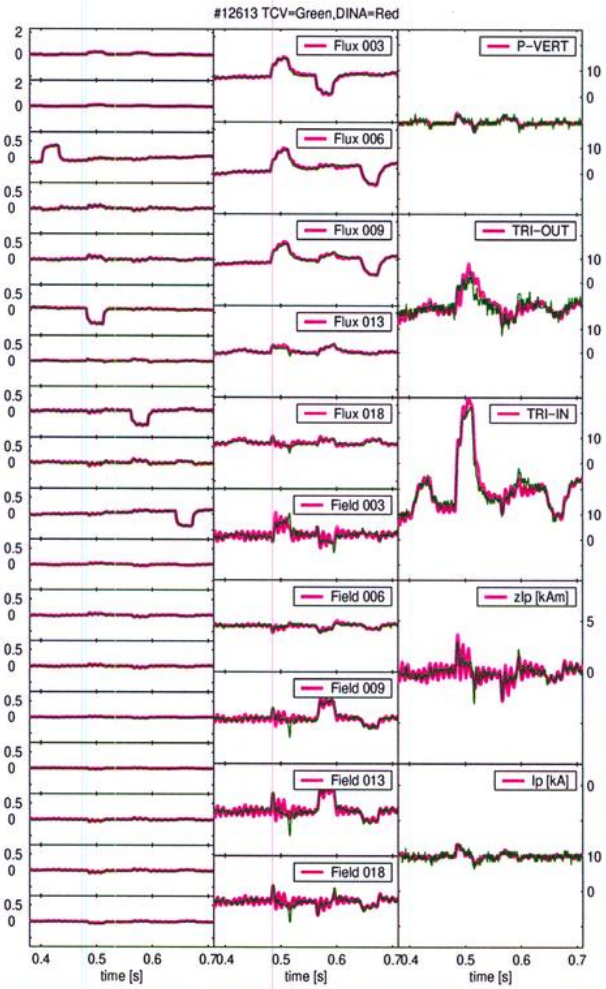

Figure 2 Simulation of a diverted off-centred plasma, using separate E1, E4, E6, E8 coil stimulations in a single pulse. The signals are shown detrended: (left column) all 18 external PF coil currents, OH1, OH2, E1 to E8, F1 to F8; (middle column) flux loops #3,6,9,13,18, magnetic probes #3,6,9,13,18; (right column) the five feedback control parameters.

results is almost always within the noise width of the experimental data.
A complete single null diverted plasma discharge was also successfully simulated. The most significant difference was the penetration time of the poloidal flux, leading to a delayed onset of sawtoothing in the DINA simulation than in the experiment, Fig.3. Since the plasma loop resistance has been adjusted to the experimental data, this implies that the initial penetration of the poloidal flux does not follow the toroidal resistivity and that care should be taken in using this assumption when investigating the plasma current ramp-up phase.
Square pulse voltage stimulation of the OH1 and OH2 coils led to oscillations during the shape excursions, not reproduced by linear simulations, seen in Fig. 4 for the OH1 response. The oscillations seen in the vertical position are well reproduced by the DINA simulation. The envelope increases around 400msec, showing that the TCV closed loop has gone unstable, with a growth time of 200-400msec. After 100msec, the oscillations become damped, when the closed loop is stable again. This change in closed loop stability is attributable to the increased vertical field decay index which causes an excursion of the plasma elongation. The increase of elongation from 1.45 to 1.53 occurs when the closed loop

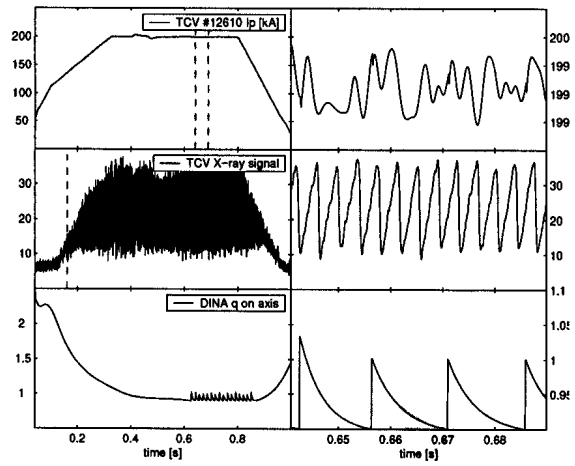

Figure 3 Comparison between DINA simulation and TCV for the evolution of the sawtooth activity: left, the full pulse showing, from top to bottom: TCV Ip, TCV soft X-ray signal, DINA q(0); right, an expanded view of the same signals.

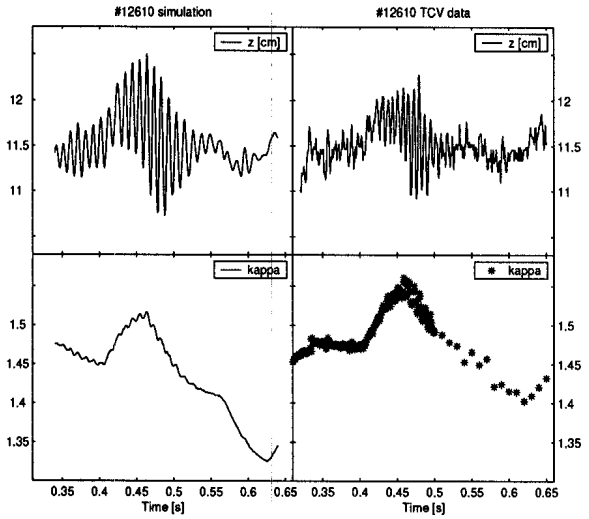

Figure 4 Comparison between TCV (left) and the DINA simulation (right) for a large excursion due to a square voltage pulse OH1 stimulation. The vertical position goes closed loop unstable and returns to closed loop stable once the elongation is reduced.

is unstable. This observation is an example of non-time-invariant behaviour of the experiment and the simulation, which can never be simulated by linearised models, for which time invariance is assumed.
The complete set of 18 frequency stimulation experiments used to measure the open loop TCV plasma equilibrium response was also simulated in DINA and the results were analysed in an identical fashion to the experimental data. We used the coil voltages rather than the PF power supply demand voltages as the input signal, since this change actually renders the analysis more sensitive to differences between models, although being more noise prone. The frequency response of the DINA simulations agreed with the experimental results.

JT-60U Experiments: The method used on TCV to measure the open-loop plasma equilibrium response during the closed-loop control of the vertically unstable plasmas has been repeated on JT-60U. The RZIP model of JT-60U was created using a cleaner Lagrangian approach. This removed an asymmetry in the determining equations concerning the radial derivative of the plasma resistance, but left most terms unchanged, see below. A series of experiments was then performed with no plasma, in an Ohmic plasma and an NBI-heated plasma, using multi-sine excitation of the 5 PF coil voltages in the range 4-80Hz, to determine the dynamic response of all diagnostics. The plasma-less model was fine-tuned to compensate for external circuitry and any constructional differences, to a precision beyond simple measurement accuracy. This procedure was necessary to avoid biasing the measurements with plasma and attributing any differences to plasma model errors. The open-loop plasma response agreed well with the RZIP model, except for the plasma current response. Varying the plasma resistance derivative in the model showed that this term is not experimentally determined in these experiments. Calibrating the values of the plasma inductance and plasma resistance in the model to agree with the experimental data showed that the effective resistance is much higher than the loop resistance and that the effective inductance is somewhat lower than the low frequency inductance. It is assumed that these observations can be explained by a skin-effect.

$$\begin{bmatrix} L_s & \left.\frac{\partial M_{sp}}{\partial z}\right|_0 & \left.\frac{\partial M_{sp}}{\partial R}\right|_0 & M_{sp}^0 \\ \left.\frac{\partial M_{sp}}{\partial z}\right|_0 & \left.\frac{\partial^2 M_{sp}}{\partial z^2}\right|_0 \frac{I_s^0}{I_p^0} & \left.\frac{\partial^2 M_{ps}}{\partial z \partial R}\right|_0 \frac{I_s^0}{I_p^0} & 0 \\ \left.\frac{\partial M_{ps}}{\partial R}\right|_0 & \left.\frac{\partial^2 M_{ps}}{\partial z \partial R}\right|_0 \frac{I_s^0}{I_p^0} & \left(\frac{1}{2}\left.\frac{\partial^2 L_p}{\partial R^2}\right|_0 + \left.\frac{\partial^2 M_{ps}}{\partial R^2}\right|_0 \frac{I_s^0}{I_p^0}\right) & \left(\left.\frac{\partial L_p}{\partial R}\right|_0 + \left.\frac{\partial M_{ps}}{\partial R}\right|_0 \frac{I_s^0}{I_p^0} + 4\pi\mu_0 \frac{S}{l^2}\beta_p^0\right) \\ M_{ps}^0 & 0 & \left(\left.\frac{\partial M_{ps}}{\partial R}\right|_0 \frac{I_s^0}{I_p^0} + \left.\frac{\partial L_p}{\partial R}\right|_0 + 4\pi\mu_0 \frac{S}{l^2}\beta_p^0\right) & L_p^0 + 4\pi\mu_0 \frac{S}{l^2}\beta_p^0 R^0 \end{bmatrix} \dot{\vec{x}} +$$

$$\begin{bmatrix} \Omega_s & 0 & 0 & 0 \\ 0 & 0 & 0 & 0 \\ 0 & 0 & 0 & \left.\frac{\partial \Omega_p}{\partial R}\right|_0 \\ 0 & 0 & \left.\frac{\partial \Omega_p}{\partial R}\right|_0 & \Omega_p^0 \end{bmatrix} \vec{x} = \begin{pmatrix} \delta V_s \\ 0 \\ -2\pi\mu_0 \frac{S}{l^2} I_p^0 \dot{\beta}_p \\ -4\pi\mu_0 \frac{S}{l^2} I_p^0 R^0 \dot{\beta}_p \end{pmatrix}$$

The resulting agreement is shown in Fig. 5 for the most important responses, namely the control parameters. The plasma-less response is shown as black crosses and the plasma responses as red and blue circles. The RZIP model is shown as solid lines of the same colours. Finally, the closed loop operation of JT-60U was successfully simulated using the RZIP model and fine-tuning the controller to reduce some of the residual cross-coupling has started.

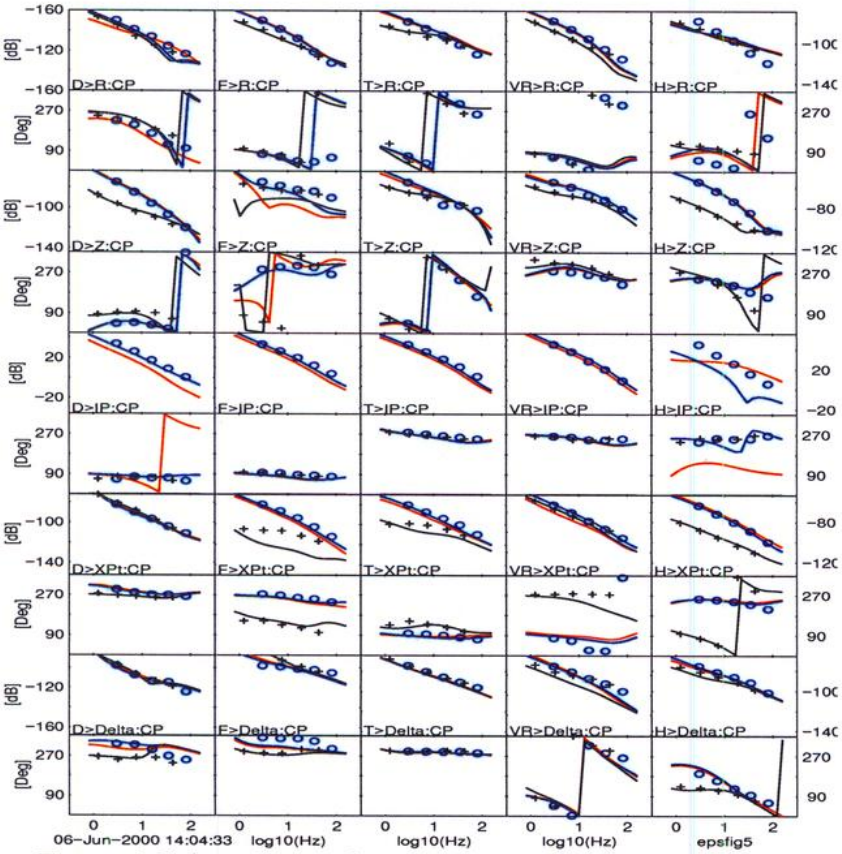

Figure 5 Selected open-loop responses from the JT-60U tokamak

Acknowledgements:

Thanks go to the TCV and JT-60U teams without whom the experimental results would not be comparable with the models. Two of the authors (RK, VL) thank the CRPP for their hospitality during visits to TCV. Two of the authors (JBL, AS) thank JAERI-Naka for their hospitality during visits to JT-60U. This work was partly supported by the Swiss National Science Foundation. One of the authors (JPW) was partly supported by the United Kingdom EPSRC.

Ohmic H-mode Accessibility in Shaped TCV Plasmas

Y.R. Martin, B.P. Duval, J.-M. Moret, J.Rommers

Centre de Recherches en Physique des Plasmas
Association EURATOM - Confédération Suisse
Ecole Polytechnique Fédérale de Lausanne
CH-1015 Lausanne, Switzerland

INTRODUCTION

Future fusion reactors like ITER are planned to operate in the ELMy H-mode regime. The H-mode is desired because of its high confinement properties and ELMs are necessary to control the plasma density and plasma impurities. ELMs, however, represent a threat to the divertor plates because of the deposited heat flux if the delay between ELMs becomes too large. Therefore, the identification of the plasma parameters which can control the ELM frequency is necessary. The strong shaping capabilities of TCV can be used to investigate the effect of plasma shape and position with plasma parameters on the ELM activity. On TCV, additional heating can not, as in other machines [1, 2 and references therein], be used to access a desired ELMing regime. Thus, other machine or plasma parameters must be found.

H-mode have already been obtained in ohmic TCV discharges with a large variety of plasma shapes, currents and densities. A large number of these discharges had an ELM free H-mode phase while some, seemingly similar discharges, exhibited ELMs. The goal of this study was to determine the conditions necessary for the production of a stable ELMy H-mode. These discharges could subsequently be used to study the plasma behaviour and ELM dynamics in an ELMing regime.

In this initial investigation, the plasma current, density, elongation, triangularity and plasma to wall gaps were scanned whilst keeping the toroidal magnetic field at its nominal value of 1.4T. A single null divertor with the ion grad B drift directed away from the X point was chosen for these experiments. This configuration has been extensively used in previous experiments and led to most of the ELMy discharges previously observed on TCV. An ELM free H-mode period on TCV results in the plasma density increasing until the discharge terminates by a high density disruption. Since many such discharges had already been obtained, plasma parameters leading to this regime could be avoided. In the same way, discharges in this configuration which remained in L-mode were also avoided. From database studies of TCV discharges, ELMs were expected for plasma parameters between these limits.

It was found that an ELMy regime could be obtained by passing through a small but well defined region of the operational domain. Surprisingly, large changes in the machine conditioning, (including a boronisation) did not significantly affect the position of this "gateway" which was used to reliably access an ELMy TCV regime (see next section). Once in the ELMy regime, the plasma was found to be relatively robust to changes in the current, shape and density. It was thus possible to access a wider range of plasma parameters whilst remaining in an ELMy regime. A subsequent section describes the operational boundaries of the established ELMy regime and the limiting operational parameters.

THE "GATEWAY" TO THE OHMIC ELMING REGIME

This section first presents how the boundaries of the ELMy "gateway" were determined. The plasma discharges in this study were tagged with one of the labels: ELMY for stationary ELMy discharges, LMODE for discharges remaining in L-mode, ELMFREE for discharges which transited to an ELM free phase, ELMYL and ELMYELMFREE were attributed to discharges alternating between the two modes and ELMY-FAIL was attributed to discharges disrupting shortly after the transition, for which the mode was unknown. Example discharges for these labels are shown in Fig. 1. The non stationary ELMing discharges were classified in two categories: discharges which ceased to be ELMy soon after the L-H transition and discharges whose ELM frequency became irregular as a result of programmed changes in some of the plasma parameters (Fig 2).

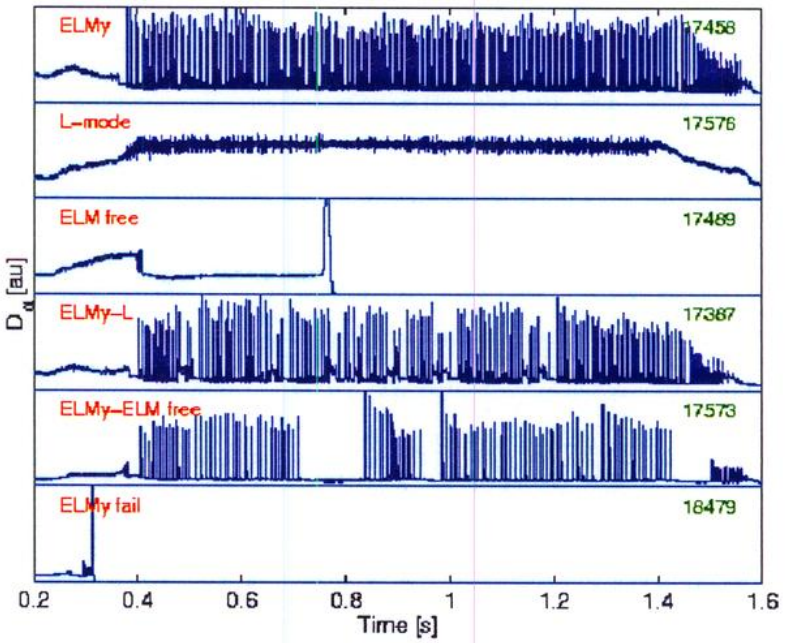

***Figure 1**: Time evolution of the D_α emission from different type of discharges as indicated on the left.*

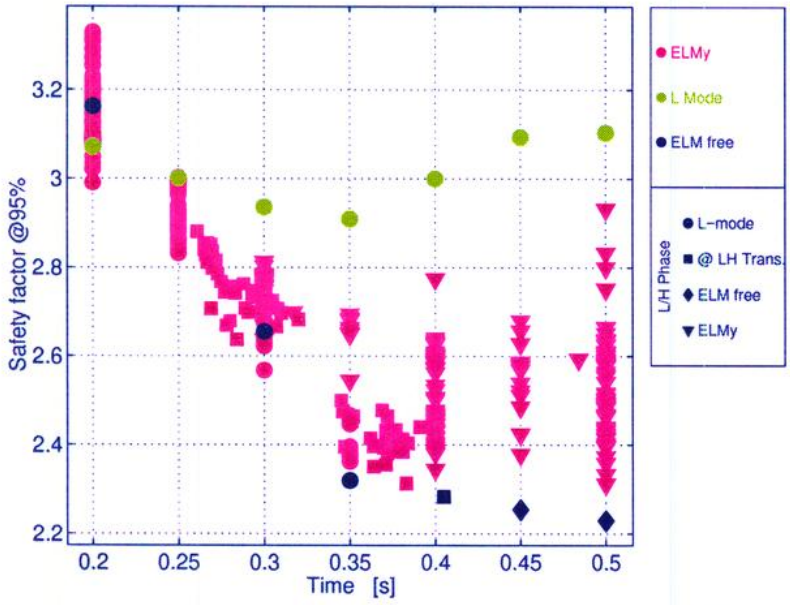

***Figure 2**: Time evolution of the safety factor for ELMy L-mode and ELM free shots indicating the available range in q_{95} for accessing the ELMy regime.*

To pass the "gateway" to the ELMy regime, three parameters must simultaneously exceed a threshold value to obtain an H-mode: a) the plasma current has to be greater than 350kA or equivalently q_{95} must be lower than 3.0 with κ=1.6-1.7 and δ=0.5-0.6 as shown in Fig. 2; b) the plasma line average density must exceed $4.5 10^{19} m^{-3}$; c) the distance between the plasma and the tiles must be greater than 1cm. The inter-dependencies between these limits were small. With the same plasma shape parameters, the plasma cur-

rent must not exceed 430kA (or q_{95}<2.3) otherwise the transition leads to an ELM free phase. A high density (> $6.10^{19}m^{-3}$) at the transition also led to an ELM free phase.

LH transitions were also provoked at higher plasma elongation (in the range 1.7 to 2.1) by retarding the formation of the SND configuration. In otherwise similarly shaped plasmas with similar densities, the L-H transition was obtained at higher q_{95}, with roughly equal values of I_p. However, these transitions led to ELM free H-modes. A reduction in the plasma density at the L-H transition time resulted in L-mode discharges. Minor changes in the plasma shape at higher q_{95} sometimes resulted in ELMs but with low frequency and high amplitude. The resulting perturbation in the control system was sufficient to lose vertical plasma position control and a disruption (VDE) ended the discharge. Changes in the control observers are being developed to improve this situation [3] which, for this paper, limited the maximum plasma elongation.

In summary, the "gateway" to the ohmic ELMy is bounded by the following limits in the operational parameters :

	I_p [MA]	$n_e[10^{19}m^{-3}]$	κ	δ	gap_{pl-w}[m]
Min	0.35	4.5	1.6	0.5	0.01
Max	0.43	6.0	1.7	0.6	0.03

THE OPERATIONAL DOMAIN OF THE OHMIC ELMY REGIME

Once in the ELMy regime, it was then possible to modify certain plasma parameters while preserving the ELMs. The plasma elongation was increased to κ=2.1, with q_{95} approximately constant, as shown in Fig. 3a. Changes in q_{95} during the elongation ramp resulted in vertical stability problems. Decreases in q_{95} lowered the ELM frequency, as mentioned above, whereas increases in q_{95} made the plasma less vertically stable. Moreover, the plasma current must

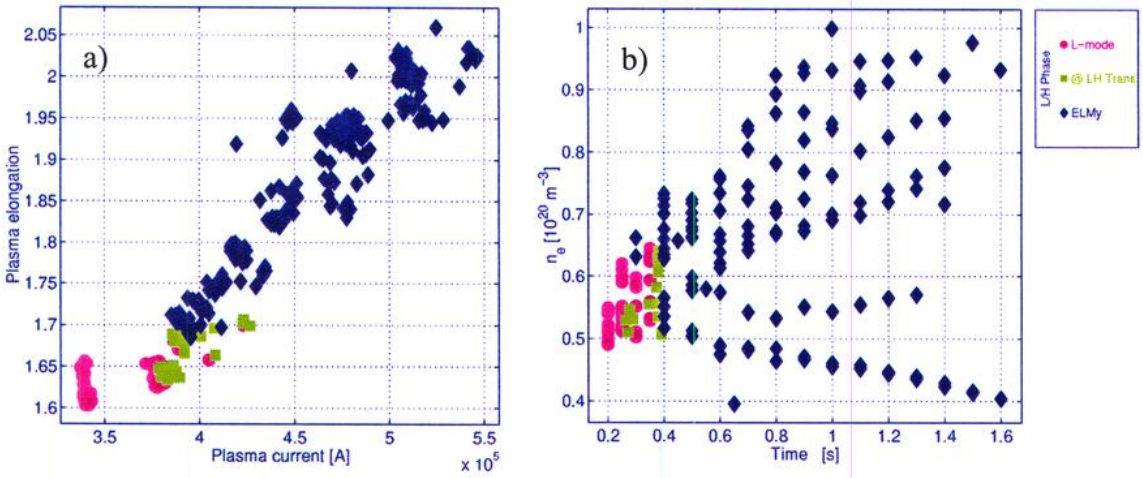

***Figure 3**: a) Accessible plasma current and elongation for the ELMy H-mode. b) Accessible plasma density for the ELMy H-mode. In both cases these parameters may only be obtained after passage through the ELMy "gateway".*

be ramped sufficiently slowly, or the discharge showed spontaneous H-L-H transitions regime or even returned to L-mode for higher values of dI_p/dt.

Once in ELMy H-mode, the plasma density could be decreased or increased in the range between 4-10.$10^{19}m^{-3}$. A strong gas puff led to alternating ELM free and ELMy phases and reducing the density finally led to a return to L-mode.

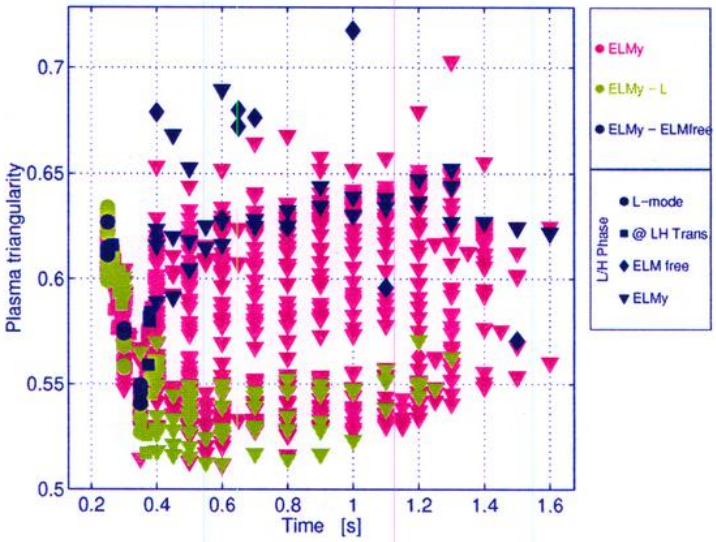

***Figure 4**: Time evolution of the triangularity for different discharges. It shows that low triangularity may lead to ELMy-L oscillations, whilst increasing the triangularity led to ELM free H-mode.*

Finally, small modifications of the plasma triangularity led to changes in the ELM accessibility (Fig 4). A relatively small increase in the plasma triangularity led to alternating ELMy and ELM free phases whereas a slight reduction in the triangularity resulted in stable discharges with frequent transitions to L-mode.

CONCLUSION

A reliable ELMy H-mode regime was successfully obtained in TCV. Access to ELMy discharges was only possible for a small region of the operational domain. Once this "gateway" is traversed, the ELMing state is stable to changes in the operational parameters. Plasma elongations from 1.6 -> 2.1, and densities from 4 -> 10 $10^{19}m^{-3}$ were successfully attained by passing the L-H transition with the "gateway" parameters and then programming plasma control changes. Although the ELM frequency was modified for these discharges, the ELMy regime characteristics were conserved. The triangularity was limited between 0.5 and 0.6 with the discharge transiting to an ELM free phase for higher triangularity and to ELMy-L regime for lower triangularity. It may be possible to extend this range by compensating these effects with changes in other plasma parameters.

The reliable access to the ELMy regime on TCV opens the way for the study of ELM dynamics and plasma confinement in this regime, both with and without ECH as a function of the plasma shape.

AKNOWLEDGEMENTS

This work was partly supported by the Fonds National Suisse de la Recherche Scientifique. This work would not have been possible without the support of the entire TCV team.

REFERENCES

[1] H. Zohm, Plasma Phys. and Contr. Fusion 38 (1996), 105.
[2] W. Suttrop, Plasma Phys. and Contr. Fusion 42 (2000), A1.
[3] F. Hofmann et al, this conference.

Improved central confinement by current profile modification in shaped plasmas using ECRH and ECCD in TCV

Z.A. Pietrzyk, C. Angioni, R. Behn, S. Coda, T.P. Goodman, M.A. Henderson, F. Hofmann, J-P.Hogge, J-M. Moret, A. Pochelon, H. Reimerdes, O. Sauter, H. Weisen

Centre de Recherches en Physique des Plasmas, EPFL
Association EURATOM-Confederation Suisse, CH-1015 Lausanne, Switzerland

Improved Central Confinement (ICC) has been observed in TCV (Tokamak à Configuration Variable) plasmas in which sawteeth were stabilized by counter-ECCD [1]. In these cases the central electron temperature was larger by about a factor of two than with CO-ECCD or with ECRH alone. Comparison of experimental results with calculations by the PRETOR transport code indicates that sawtooth stabilization is sufficient to explain the increased confinement time and the consequent enhancement of the central electron temperature. The simulations show that sawtooth stabilization is caused by the central safety factor q_0 rising above 1 for counter-ECCD cases whereas q_0 remains below 1 in the sawtoothing CO-ECCD and ECRH cases.
ECH in TCV demands a low plasma density (the cutoff for an 82.7GHz wave is $4.25 \cdot 10^{19} m^{-3}$). Under these conditions and particularly during the electron heating phase, the ion temperature is much smaller than the electron temperature. Thus the Rebut-Lallia-Watkins (RLW) scaling law constitutes an appropriate reference for the electron energy confinement time. The experimental confinement time in ICC shots is more than 3 times higher than the global RLW scaling and is often well reproduced by PRETOR, even though PRETOR is based on the local RLW diffusivity model. Hence, current profile modification - rather than a change in the transport coefficients - is chiefly responsible for the enhanced confinement. The exceptions are shots with "prepared" low χ_e values in the central part of plasma for which experimental profiles are broader than calculated by PRETOR (see below).
Sawteeth can be more easily stabilized at low elongation (κ) and large edge safety factor (q_a). Successful stabilization has been observed with 1.35MW counter-ECCD in the plasma centre. Fig. 1 shows a comparison of temperature profiles with counter-ECCD, co-ECCD and ECRH, all with central power deposition. The maximum enhancement factor H_{RLW} in the counter case is 3.5, while it is 1.5 during co and ECRH.

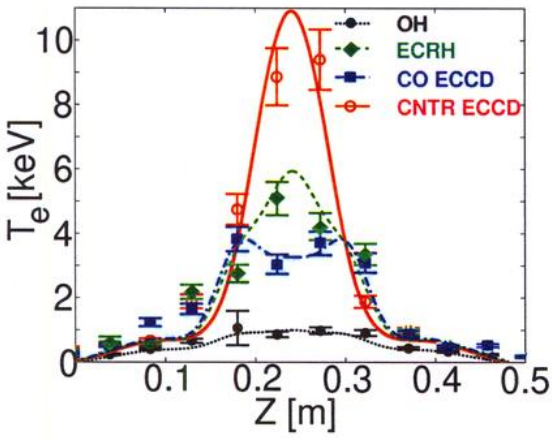

Figure 1. Electron temperature profiles along a vertical cord with counter- co - ECCD and with ECRH. An Ohmic case is shown for reference. Central power deposition. κ=1.2, δ=0.2, q_a=5.5, 1.35MW

In a more recent campaign, with additional power a larger domain of κ (up to 2.2) and q_a (down to 2.4) was investigated. Results from a plasma with κ=1.6-1.8 are shown in Figure 2, which compares two shots with counter-ECCD at the plasma magnetic axis. Confinement expressed by the H_{RLW} enhancement factor, is quite good in both cases in spite of MHD mode activity.

The ray tracing (TORAY) calculations shown are based on T_e and n_e experimental profiles. The beams are 100% absorbed in the yellow region and no power is transmitted to the black region.

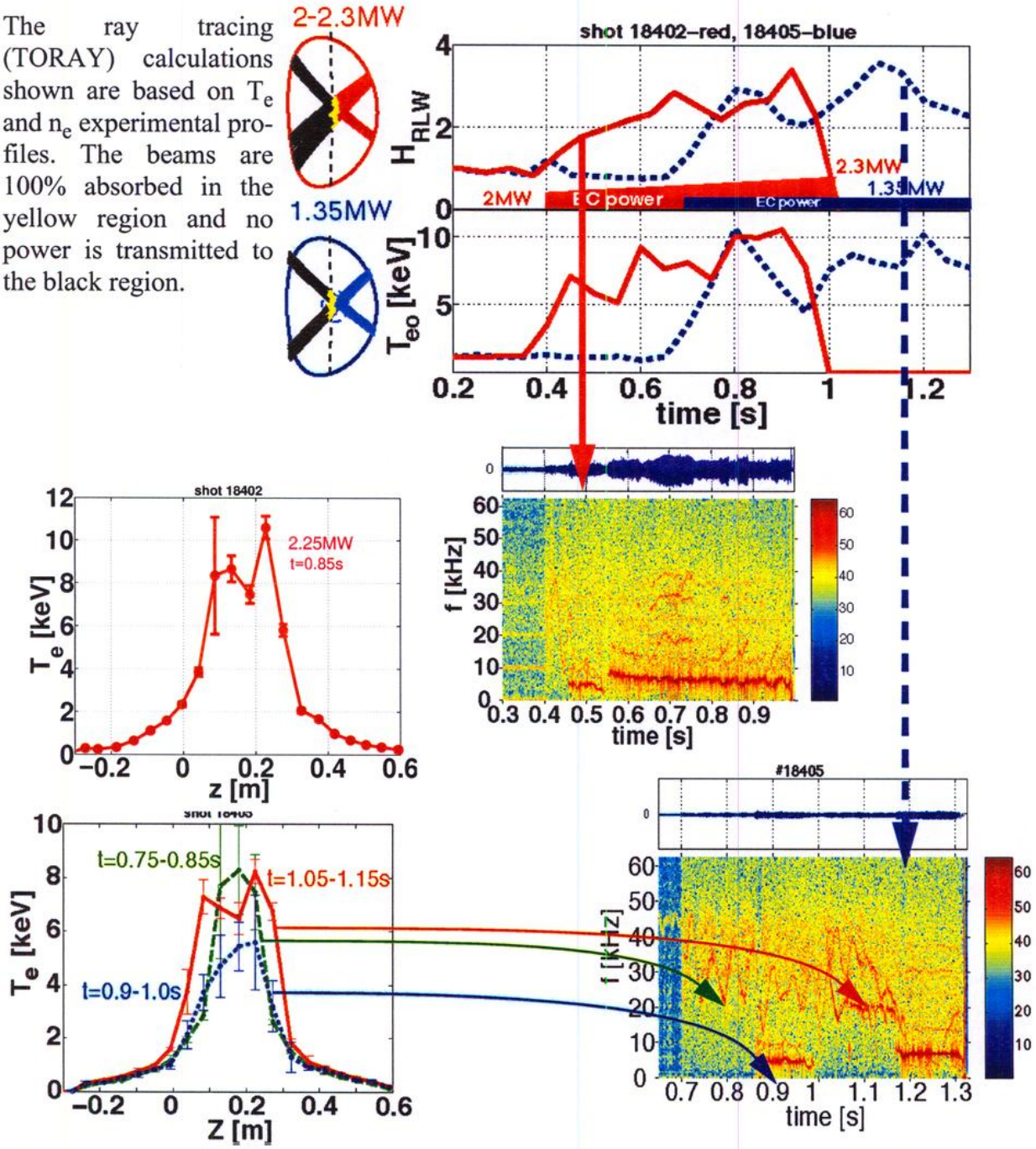

Figure 2. Comparison of two shot: one (18402) with a power ramp from 2 to 2.3 MW followed by plasma disruption, the other (18405) with 1.35MW constant power (both with counter- EC-CD). Shot 18402: κ=1.8, δ=0.3, q_a=9; shot 18405:κ=1.6, δ=0.25, q_a=7. The difference in parameters between the shots is not intentional.

However, the confinement time improves further when the low-frequency mode (~5kHz) is absent; indeed both H_{RLW} and the central temperature are well correlated with the existence of low frequency mode.In some cases it has been observed that the period of improved confinement is suddenly terminated, which is visible as a rapid decrease of the soft x-ray emissivity and collapse of the central temperature [1]. This collapse is due to an instability, since the temperature collapse is correlated with an increase in mode activity. From an analysis of magnetic probe data we could identify a high m-number mode. However, this mode is most likely coupled to an internal m=1 mode as the central temperature collapse at the appearance of this high m-number mode.

This catastrophic temperature collapse can be prevented, at least in some cases, by increasing the power in the centre gradually.
In the high κ and high q_a regime at low power there appear to exist two regimes of a good confinement as seen in Fig. 2. The time evolution from the first to the second regime is rather complex. The initial good confinement is reduced at the appearance of the mode and the central average temperature drops from 8 to 5 keV. Since the mode appears after a time of the order of the current redistribution time (~150ms), we speculate that the profile becomes too peaked and triggers instability. It is, however, unclear how the mode is stabilized later to produce a second good confinement regime with a broader temperature profile, but lower plasma density. This second good confinement regime is in turn destroyed by another mode. At higher power (2MW) and with the same central power deposition the mode starts earlier (50ms after turn on ECH). In the presence of the mode, the confinement enhancement factor appears to increase with power. The width of the temperature profile indicates that in this case we are already in the second good confinement regime. Thus, higher power can produce good confinement even in the presence of the low frequency mode.

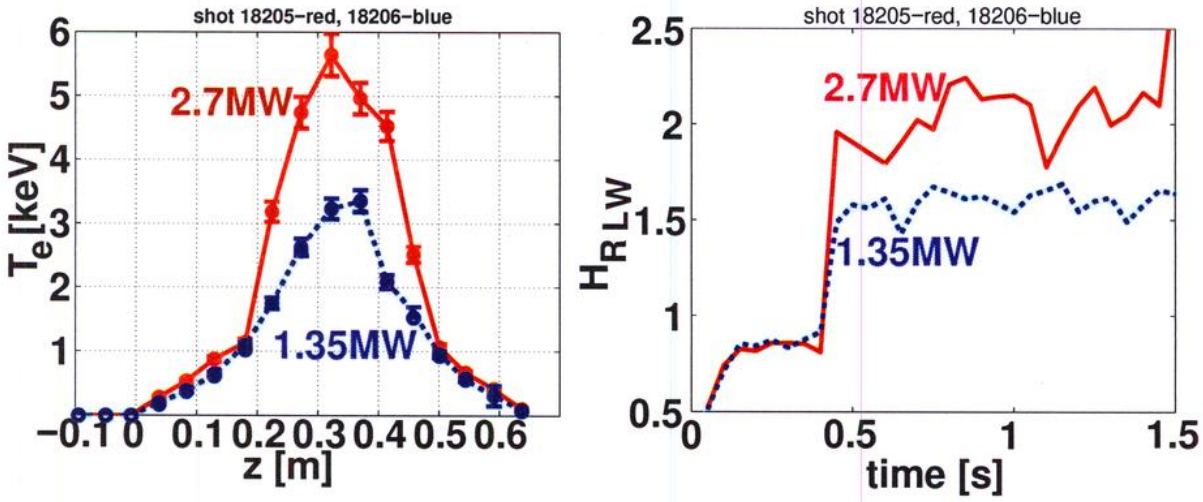

Figure 3. Changes in the temperature profile and H_{RLW} factor with power for counter-ECCD with power deposition near the magnetic axis and low q_a: κ=1.2, δ=0.19, q_a=3.1

Finnaly, we have also found that the electron energy confinement is better with counter ECCD than with ECRH with central power deposition even if the sawteeth are present. In this case the H_{RLW} factor increases with power as shown in Figure 3.

The mode activities are more easily suppress if part of power is deposited off axis either CO ECCD or ECRH mode (which one is better depends on plasma conditions). However, the enhancement factor H_{RLW} does not increase and in fact rather decreases. One of these cases (shot 18224) is shown in Fig. 4 along with a shot with all co ECCD in the plasma centre for comparison. (In shot 18224 the power was changed by a factor of two during the shot). In the shot with all co ECCD (shot18200) the plasma temperature is not as high, but energy confinement is good and the plasma is stable and sawtoothing. This shot has also a very good H_{RLW} factor of 2.5, only slightly smaller than for the case with counter on axis and 2.7MW power, but the central temperature is significantly lower.

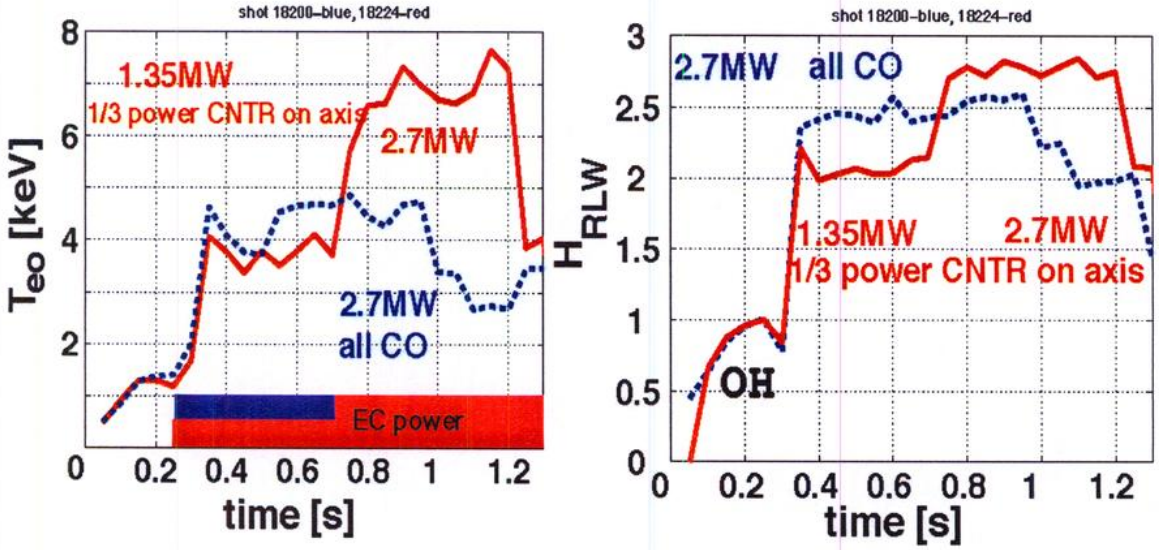

Figure 4. Shots with distributed power deposition: shot 18200 with all beams in CO ECCD direction (dashed blue), shot 18224 with two central beams in counter-ECCD direction and four off axis beams in CO direction (solid red). κ=1.6, δ=0.29, q_a=7.

The best results, so far have been observed using a scenario with power deposited in two steps ("prepared" low χ_e scenario). During the first step off axis heating or co ECCD is used to modify the current profile and obtain low (lower than Ohmic) χ_e in the central part of plasma. After a delay time (several 100ms), additional power is added in the plasma centre using counter ECCD configuration. In the first phase, with 1.35MW EC power the plasma temperature reaches 2keV and χ_e drops by about a factor of 4, owning to the lower Ohmic power in the centre. The enhancement factor at this stage is already 1.7. When the additional power is added in the centre, the central χ_e increases, only very slightly, so that the energy confinement time actually increases with the additional power, see Fig. 5. In these shots H_{RLW} reaches a value of 4 with central temperatures above 10keV. Figure 6 shows the χ_e profiles for such a shot.

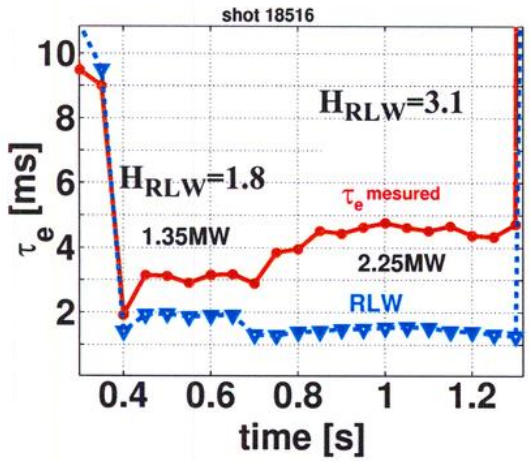

Figure 5. Electron energy confinement time for a shot with low χ_e "prepared" in the plasma centre by ECRH beams at ρ=0.4 at 0.4-0.7s

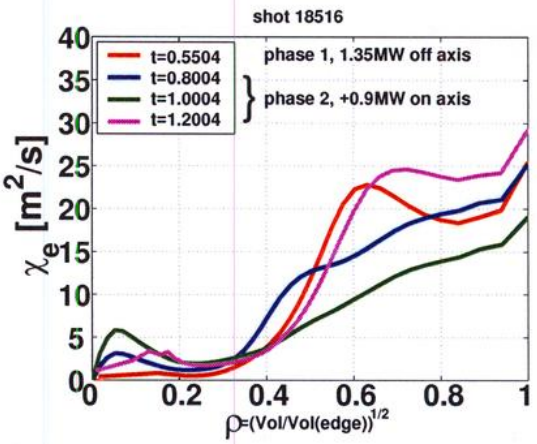

Figure 6. χ_e profiles for the shot of Fig. 5 calculated from T_e and n_e experimental profiles using the formula

$$\chi_e = \frac{-Q_e}{n_e \cdot \nabla T_e}$$

This work was partially supported by the Swiss National Science Foundation.

1. Z.A.Pietrzyk, C.Angioni et al. Physics of Plasma July 2000

Stability and Transport in Compact Quasi-axially Symmetric Stellarators

M. H. Redi[1], W. A. Cooper[2], A. Diallo[4], G-Y. Fu[1],
C. Nührenberg[3], A. H. Reiman[1], R. B. White[1], M. C. Zarnstorff[1]
and the NCSX Team

[1]*PPPL, Princeton University, Princeton, NJ 08543*
[2]*CRPP-PPB, Lausanne, Switzerland*
[3]*IPP, Greifswald, Germany*
[4]*Physics Department, University of Iowa, Iowa City, Iowa 52242*

1. Introduction

The potential performance and flexibility of a compact, quasi-axially symmetric (QAS) stellarator design [1], has been addressed by studying the effects of varied pressure and rotational transform profiles on the global, ideal magnetohydrodynamic (MHD) stability and the energetic particle transport [2]. The CAS3D [3] and TERPSICHORE [4] code packages were used in the MHD studies while the ORBITMN/ORBIT3D [5,7,2] code package was used for the transport simulations of the three field period QAS.

2. Pressure and iota profile variations

To assess robust performance in a medium-size experiment, the VMEC code [6] was used to obtain magnetic flux surfaces for 30 equilibria near the design point [1], while keeping the boundary shape and the average beta fixed at 3.8%. The plasma equilibria obtained were designated P0X/I0Y as follows: P00/I00 was the baseline configuration. P01, P02 and P03 were defined so that P01 was similar to P00, P02 was more peaked than P01, while P03 was broader than P01. P04 was a very broad, parabolic pressure profile and P05 was the pressure profile used in helias reactor studies based on the W7-X design. The iota profiles were chosen as follows: I01 was linear, maintaining $\iota(0)$ and $\iota(a)$ the same as in I00. I02 and I03 were based on I01 and also kept $\iota(0)$ and $\iota(a)$ as in the baseline case, but with edge shear increased by a factor of 1.5 and 2. I04 was a linear iota profile with $\iota(0)$ as for the other profiles, but $\iota(a)$ higher than 0.5, similar to I01. The pressure and iota profiles are shown in Ref. [2].

3. Stability of the External Kink and Periodicity-Preserving Modes

Stability calculations for the pressure and iota profile variations were made with TERPSICHORE, with a pseudoplasma approximation for the vacuum region, and a conducting wall at 1.5 minor radii away from the plasma boundary. A range of MHD behaviors was found, with a robust region of stability around the design point (see Fig. 1). The N=0 and N=1 MHD modes were destabilized by steep pressure gradients, depending on the iota profile. Figure 1 shows how the stability of the N=1 external kink mode depends on the pressure and iota profiles. For pressure profiles P00 and P04 the unstable modes found were similar for all the iota profiles. Global kink modes were generated by steeply peaked profiles near the half-radius and edge localized kink (ELK) modes were found if the edge iota was above 0.5 and if there was a steep edge pressure gradient. These ELKs in the QAS were driven by high edge current densities, as are the edge localized modes (ELMs) in tokamak H-mode plasmas.

CAS3D extended TERPSICHORE's calculations to equilibria with no conducting wall. Figure 2 shows the global kink instability as calculated by both TERPSICHORE and CAS3D for P02/I00. Figure 3 shows the CAS3D result for beta above the design point: the marginally unstable N=1 eigenfunction for P00/I00 at 3.9% beta for the case where the conducting wall is at infinity, too far away for stabilization.

Figure 4 shows the destabilization of the kink mode eigenvalue with increasing beta, as calculated by the two MHD stability codes. Here the beta was scaled with increasing toroidal plasma current. The N=1 kink mode is calculated by the CAS3D2.vac module of CAS3D, with a conducting wall at infinity, to be stable below beta approximately 3.9% (solid circles). TERPSICHORE (open squares), with a conducting wall at 2.5a from the plasma edge, finds a higher value for the critical value of beta at which the N=1 kink mode remains stable, namely 4.03%. Convergence studies confirm these results. The kink mode is stabilized by a nearby conducting wall for QAS stellarators, as for tokamaks. A simple model is being developed for stabilization of the external kink in QAS.

4. Energetic Particle Transport

Neutral beam ion losses for hydrogen beams at B=2T are calculated to be 25% after one slowing down time, using a new complete test particle collision model in ORBIT3D. This is in good agreement with recent calculations [1], and in contrast to our earlier work which used a simpler collision model [2, 7]. We find little effect on the energetic particle loss from the variations in plasma pressure and iota [2]. Among the different equilibria, the variability in the energetic particle loss was less than ±15% that of the design point, confirming the robustness of the energetic particle confinement in the QAS plasmas.

5. Conclusions

A series of simulations and calculations varying the pressure and iota profiles for a compact QAS design shows that there is stability of the N=1 and N=0 kink mode near the design point, with kink mode destabilization possible, depending on the pressure and iota profiles chosen. These calculations for edge poloidal flux, plasma boundary shape and beta kept constant also demonstrate that many of the concepts of tokamak MHD are useful in understanding how instabilities arise in QAS. Agreement of the stability codes gives confidence in the calculations of both, for predicting accurately the performance of future experimental devices. We find the CAS3D and TERPSICHORE codes give good agreement in calculations of the critical beta below which the external kink mode is stabilized. The two codes show the same identification of the poloidal and toroidal harmonics (m,n) and same radial behavior of the largest Fourier components of a global N=1 kink instability when the pressure profile is steep near the plasma half radius, as well as stability for less steep pressure profiles. Good stability is found from both codes which use different models to describe the vacuum plasma and assume different distances between the plasma and the conducting wall.

Energetic particle loss is acceptable, including collisional stochastic losses, with little change when the equilibrium is varied. Robust and flexible performance is found for this compact, quasi-axially symmetric candidate plasma being considered for the National Compact Stellarator Experiment (NCSX).

6. Acknowledgement

We thank R. J. Hawryluk, and G. H. Neilson, Princeton Plasma Physics Laboratory, for encouragement and support. We also thank H. Mynick, N. Pomphrey, J. Manickam and D. Monticello at Princeton Plasma Physics Laboratory, and D. Spong, E. Lazarus and S. Hirshman at Oak Ridge National Laboratory for clarifying discussions.

*Supported by the US Dept. of Energy Contract DE-AC02-76CH03073.

[1] G. H. Neilson, et al., Phys. Plas. **7** (2000) 1911.
[2] M. H. Redi, et al., Phys. Plas. **7** (2000) 2508.
[3] C. Nührenberg, Phys. Plas. **6** (1999) 137. C. Nührenberg, Phys. Plas. **3** (1996) 2401. C. Schwab, Phys. Fluids **B5** (1993) 3195 .
[4] W. A. Cooper, et al., Phys. Plas. **3** (1996) 275.
[5] R. B. White and M. S. Chance, Phys. Fluids **27** (1984) 2455.
[6] S. P. Hirshman, W. I. Van Rij, P. Merkel, Comput. Phys. Comm. **43** (1986) 143.
[7] M. H. Redi, et al., Phys. Plas. **6** (1999) 3509.

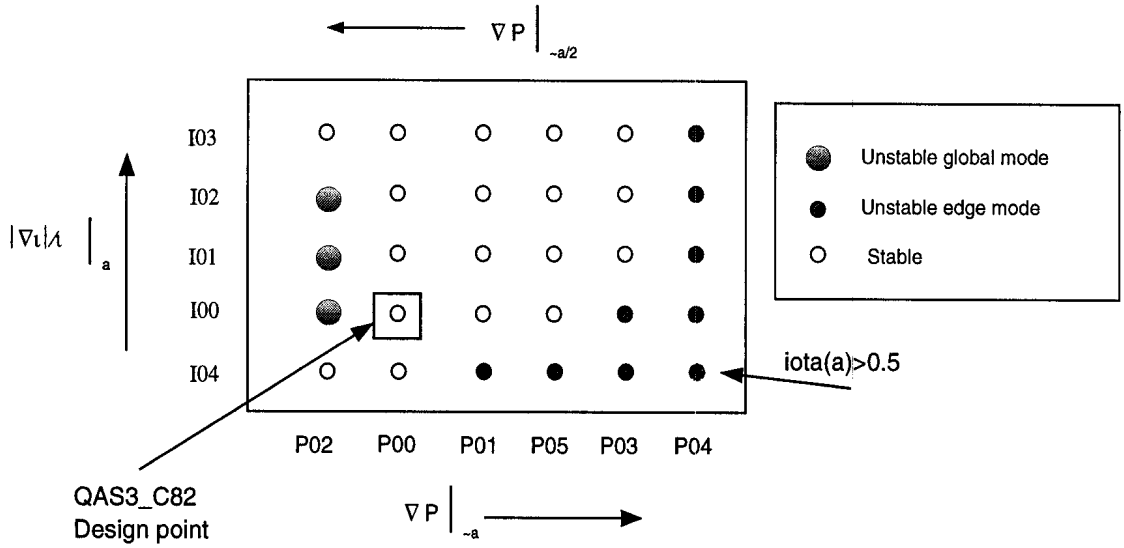

Fig. 1 N=1 family stable and unstable configurations for 30 equilibria. Stability and instability identified by the TERPSICHORE code.

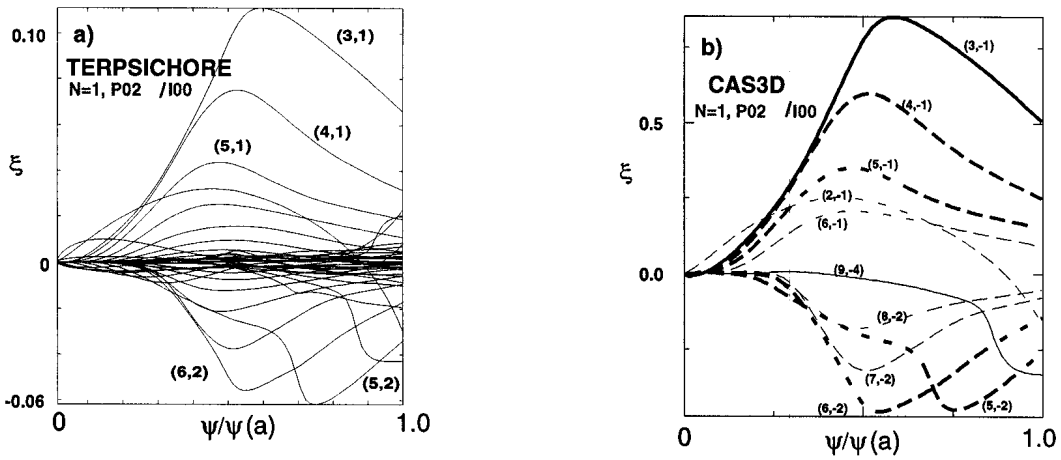

Fig. 2 The unstable external kink mode for P02/I00, 128 flux surfaces, 108 harmonic basis function modes, odd parity perturbation. ψ/ψ(a) is the edge normalized toroidal flux. Shape and identification of largest Fourier components agree in both codes.

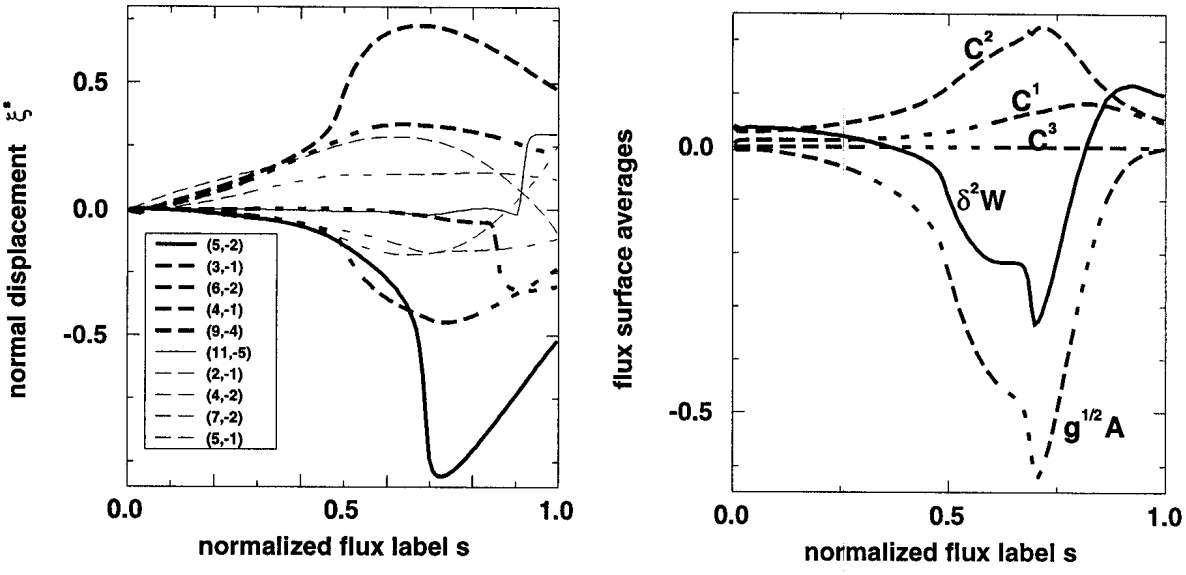

Fig. 3 CAS3D calculations for the external kink mode in the design point case P00/I00 above the design point beta, beta = 3.9%,
Left: harmonics of the normal displacment.
Right: balance of terms in the energy integral.
The perturbation is formally unstable, but very close to stabilization.
The influence of divergent parallel current densities at natural resonances (e.g. 3/8) has been eliminated. Computation parameters as in Fig. 1

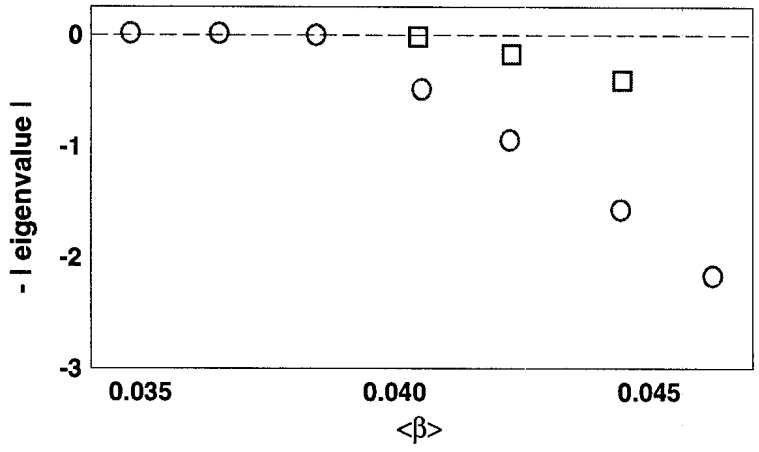

Fig. 4 Calculation of stabilization of N=1 external kink mode eigenvalue.
Open circles: CAS3D with wall at infinity; stabilization at beta ~ 3.9%.
Open squares: TERPSICHORE with wall at 2.5a, marginal beta at 4.03%.
Eigenvalues from CAS3D: λ (10^2), from TERPSICHORE λ (10^3).

Neoclassical tearing modes in TCV

H. Reimerdes, T. Goodman, A. Pochelon, O. Sauter

Centre de Recherches en Physique des Plasmas
Association EURATOM - Confédération Suisse
Ecole Polytechnique Fédérale de Lausanne, CH-1015 Lausanne, Switzerland

INTRODUCTION

Neoclassical tearing modes (NTM) have been observed in high β and low-collisionality discharges in a number of tokamaks. They often limit the achievable beta at values well below ideal MHD predictions. In contrast to conventional tearing modes, which arise from the free energy of an unstable current profile, neoclassical tearing modes are destabilized by a helical perturbation to the bootstrap current, which is generated by the flattening of the pressure profile across a seed island. The evolution of the radial island width, w, is described by the generalized Rutherford equation [1]:

$$\frac{\tau_R}{\rho_s}\frac{dw}{dt} = \rho_s\Delta'(w) + \rho_s\beta_p\left((a_{bs}-a_{GGJ})\frac{w}{w^2+w_d^2} - a_{pol}\frac{1}{w^3}\right) \qquad (1)$$

where τ_R is the resistive time on the resonant flux surface with a radius ρ_s and β_p the poloidal beta. The first term on the right hand side of (1) describes the conventional driving mechanism for tearing modes via the tearing parameter Δ', which itself depends on w. The destabilizing effect of the perturbed bootstrap current is proportional to a_{bs} and the, usually stabilizing, Glasser-Green-Johnson effect to a_{GGJ}. The threshold island width w_d is due to an incomplete flattening of the pressure profile caused by the finite heat conductivity across field lines. The term $\propto a_{pol}$ describes the neoclassical polarization current, which arises from the perturbed bootstrap current inertial response to a rotating perturbation. The effect of perpendicular heat transport and polarization currents is only important for small islands. For large islands and sufficiently negative Δ' the main stabilizing effect arises from the magnetic energy needed for the island formation. The width of the saturated island is then given by

$$w_{sat} = \beta_p \cdot \frac{a_{bs}-a_{GGJ}}{\rho_s\Delta'(w_{sat})} \cdot \rho_s \,. \qquad (2)$$

OBSERVATION OF PRESSURE DRIVEN MODES

The TCV tokamak (major radius R=0.88m, minor radius a=0.25m) is now equipped with six 82.7GHz gyrotrons, each one of them providing 500kW of electron cyclotron resonance heating (ECRH) power at the second harmonic of the extraordinary mode. In experiments using up to 2.8MW of central ECRH power, an MHD mode was destabilized a few 10μs up to more than 1s after the onset of the additional heating power. A typical launching geometry using two gyrotrons can be seen in Fig. 1(a). Both beams include a tangential component and drive current in the direction of the ohmic current. About 300ms after the switch on of the ECRH (t=0.4s) an MHD mode starts to grow and saturates at a high level (Fig. 1(b)). The degradation of energy confinement is clearly visible on a soft X-ray measurement along a central chord (Fig. 1(b)). After the switch-off of one gyrotron (t=1.95s) and the resulting drop in beta, the amplitude of the mode decreases as it is expected for the saturated island width of an NTM (2). At the switch off of the last gyrotron the amplitude quickly decreases to zero.

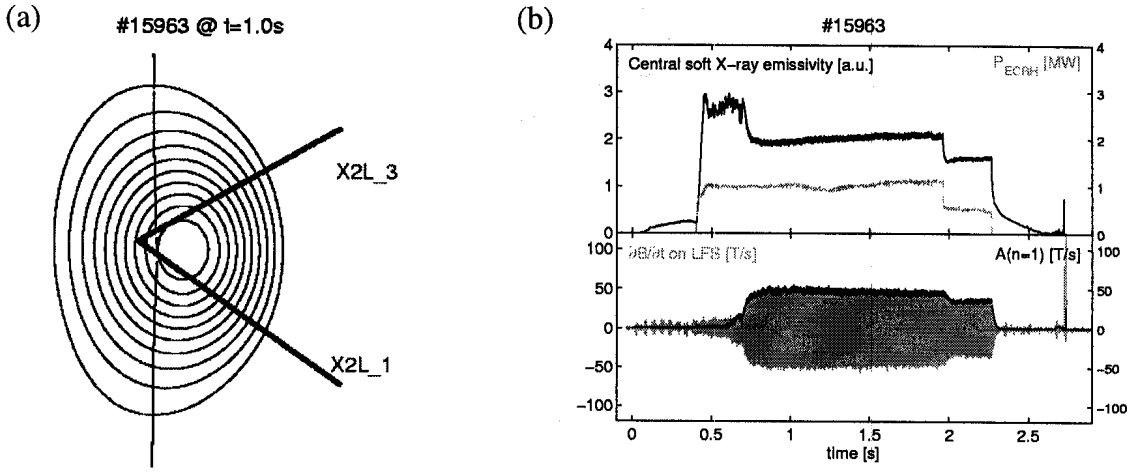

Fig. 1 (a): The poloidal plasma cross section and the ECRH launching geometry indicate a central power deposition at the second harmonic X-mode absorption layer. (b): During ECRH heating a drop in the central line integrated soft X-ray intensity is caused by an n=1 mode, which is seen in magnetic fluctuation measurements at the plasma edge.

The mode structure is determined from magnetic fluctuation and soft X-ray emissivity measurements. A toroidal array of magnetic probes identifies a dominant n=1 mode (Fig. 1(b)) rotating with 4 kHz in the direction of the electron diamagnetic drift. The poloidal mode structure is measured with an array of 38 magnetic probes in the poloidal plane. Owing to the highly elongated vacuum vessel, the interpretation of the measurements requires an inversion. The inversion method used is based on a model of a force and divergence free perturbation current along the equilibrium field lines on a resonant surface [2]. A Biot-Savart integration, using the modeled perturbation current distribution, reveals the eddy currents in the vacuum vessel and the magnetic field at the location of the pick-up coils. A comparison of phase and amplitude of the modeled mode and the measured magnetic perturbation field clearly identifies an m=2 mode. The mode is also seen in the tomographic reconstruction of soft X-ray emission measurements along 200 line-of-sights. A singular value decomposition of the reconstructed emissivity reveals an m=2 mode rotating with the same frequency. There have been also discharges showing a 3/2 mode with the same characteristics.

The island size can be calculated from the magnetic perturbation field $B_{\theta mn}$ measured at the plasma edge. In a cylindrical approximation assuming a constant perturbed flux across the island, a multipolar decay towards the edge, and an ideal conducting wall behind the probes the full island width w is given by

$$w = \left(8\left(\frac{b}{\rho_s}\right)^{m+1}\frac{B_{\theta mn}(b)}{\varepsilon_s n B_\varphi s_s}\right)^{\frac{1}{2}}\rho_s \,, \tag{3}$$

where b is the distance between the probe and the axis, s_s the magnetic shear and ε_s the inverse aspect ratio of the resonant flux surface. The reconstructed island width is shown in Fig. 2. However, this reconstruction is very sensitive to the position and the magnetic shear on the resonant flux surface and depends on the uncertainty of the equilibrium reconstruction. An independent estimate of the island size is obtained from the confinement degradation. According to the Chang and Callen belt model [3], a confinement degradation $\Delta W/W$ in a centrally heated plasma can be caused by an island with a width $w = -\frac{1}{2}(\Delta W/W)/r_s \cdot a^2$. The energy drop is obtained from the SXR-emissivity measurement along a central chord,

which is corrected for the change in density and results in an island width of 4.5cm, which is ~20% smaller than the value determined according to (3) (Fig. 2). This difference gives an estimate for the experimental uncertainty of w.

IDENTIFICATION AS A NEOCLASSICAL TEARING MODE

In order to identify the driving term of the mode, the evolution of its width w is tested against an island evolution described by the modified Rutherford equation (1). Fig. 2 shows that starting with the rapid growth at t=0.69s (corresponding to w=3cm) the evolution of the experimental island width agrees well with the prediction. Since the stabilizing effects of perpendicular transport and polarization currents decrease rapidly with w, w_d and a_{pol} were set to zero. Furthermore, Δ' was assumed to be stabilizing ($\Delta' < 0$). Since the classical ($\propto \Delta'$), and the neoclassical ($\propto a_{bs}$) driving term differ in their β_p and w dependence, the observed mode clearly shows the characteristics of a neoclassical mode. The rapid change of the saturated island width after the switch off of one gyrotron at t=1.95s is also characteristic, since β_p changes on a confinement time scale ($\tau_E \sim 5ms$) whereas Δ' changes on a longer current diffusion time scale ($\tau_R \sim 100ms$). Note, that it was not possible to obtain good agreement between the observed island evolution and the neoclassical model for small values of w, which will be discussed below.

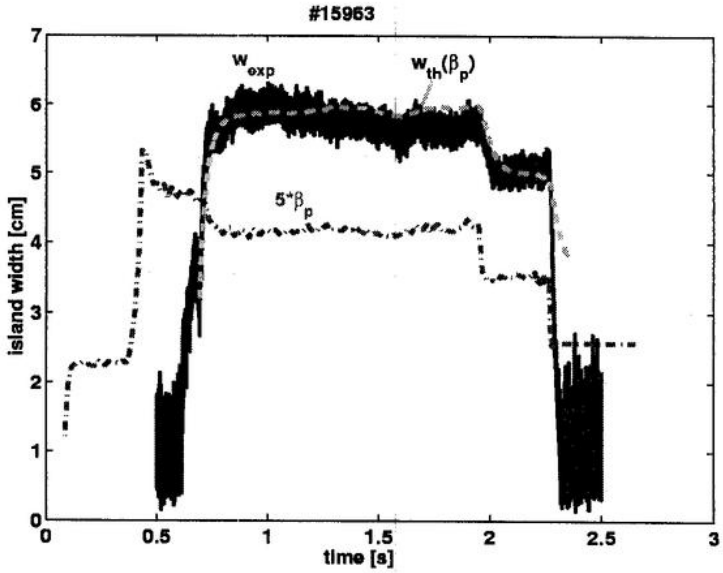

Fig. 2 The simulated evolution of a neoclassical 2/1 mode using constant coefficients and the experimental value of β_p is compared to the experimental island width derived from magnetic measurements.

ONSET OF NEOCLASSICAL TEARING MODES IN TCV

Neoclassical modes have been observed in plasmas, which were heated with 0.8 to 2.8MW of central ECRH and always included on-axis co-current drive. The central electron density at the onset of the mode ranges from 1.2 to $3.0 \times 10^{19} m^{-3}$ and is limited by runaway-electrons at low densities and by refraction of the microwave beam at higher densities. At the onset of the NTM the electron collisionality, ν_{e*}, is low ranging from 0.02 to 0.04. The normalized ion collisionality, ν_* is typically 0.3-0.5. The normalized beta, β_N, ranges from 0.4 to 1.0. These values of β_N are well below the values observed in other experiments [1]. However, the strongly localized power deposition of ECRH has been seen to generate large pressure gradients which can locally generate large bootstrap currents. If the resonant surface is located within this high gradient region, the bootstrap fraction can be sufficient to destabilize a neoclassical island. Therefore, small changes to the deposition profile can greatly influence the mode amplitude. In experiments where the deposition was moved slightly outwards the island

width decreased by 20% while beta stayed constant. A broadening of the deposition profile has suppressed NTMs in experiments where the plasma current was completely wave-driven [4]. In order to investigate the triggering mechanism the measured growth of the island is shown as a function of the island width (Fig. 3). The island has two distinct growth phases. The faster

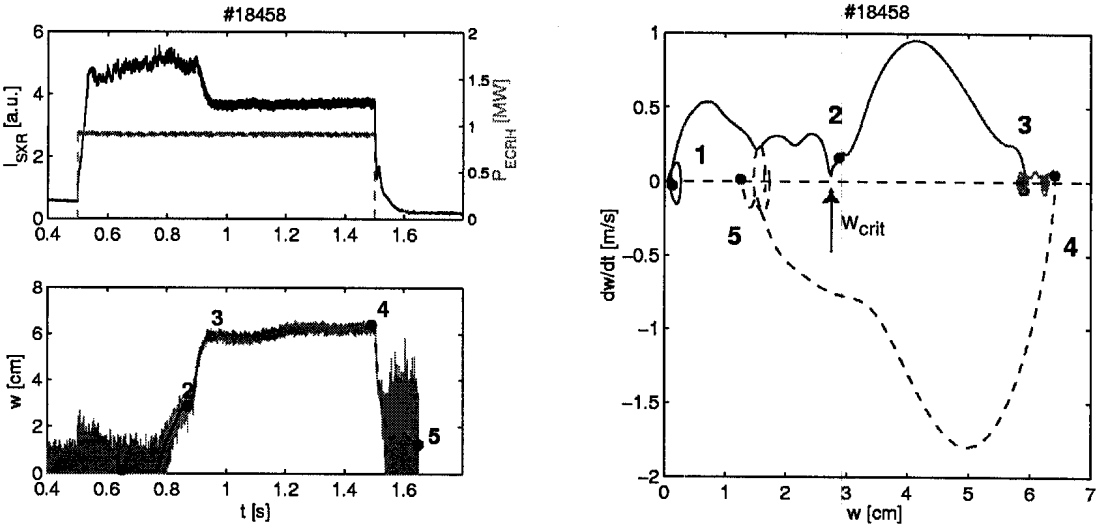

Fig. 3 The NTM is triggered by a conventional mode, which grows on a slow time scale and approaches saturation (2:t~0.87s). Once the critical island width w_{crit} is attained the mode growth on a faster time scale to its full width. After the ECRH is switched off (4: t~1.49s) the island width quickly drops (dashed line).

growth at larger mode amplitude corresponds to the neoclassical island evolution modeled for #15963 before (Fig. 2). The critical island width w_{crit} is approximately 2.8cm. It is suggested that a conventional tearing mode provides the seed island. The 2/1 mode structure shows no change between the two phases. The initial growth of 0.4m/s, which corresponds to $\rho_s \Delta' = 0.4$, decreases as Δ' decreases with *w*. The effect of Δ' is also visible at the switch-off of ECRH, when *dw/dt* drops with β on an energy confinement time scale to the value determined by Δ'. At such large values of *w*, Δ' is strongly stabilizing, but slowly increases with decreasing *w*. At *t*=1.6s it is close to its value prior to the onset of the mode.
The triggering by a conventional tearing mode explains the peculiar conditions under which NTMs were observed in TCV. Since the discharges also have to be unstable with respect to classical tearing, NTMs are only triggered in discharges where on-axis current drive generates peaked current profiles. A sawtooth induced seed island like they are observed on other experiments seems unlikely since they would not be sufficiently large to exceed the observed w_{crit}, which corresponds to approximately 10% of the minor radius.

ACKNOWLEDGEMENTS

This work was partly supported by the Swiss National Science Foundation.

References

[1] Sauter O *et al* 1997 *Phys. Plasmas* **4** 1654 and references therein
[2] Schittenhelm M, Zohm H and ASDEX Upgrade team 1997 *Nucl. Fusion* **37** 1255
[3] Chang Z and Callen J D 1990 *Nucl. Fusion* **30** 219
[4] Sauter O *et al* 2000 *Phys. Rev. Lett.* **84** 3322

RF plasma deposition uniformity on square-meter substrates

L. Sansonnens, A.A. Howling, J. Ballutaud and Ch. Hollenstein
Centre de Recherches en Physique des Plasmas
Ecole Polytechnique Fédérale de Lausanne
CH-1015 Lausanne, Switzerland

Introduction

Plasma assisted deposition or etching of thin solid films such as amorphous silicon or silicon oxide has widespread applications, especially in the field of photovoltaic solar cells and thin film transistors for flat screen production. Industrial applications require high deposition rates over large areas (up to a square meter) with a layer thickness uniformity to better than 5% for flat screens and about 10% for solar cells. The radio-frequency parallel-plate plasma reactor is the most commonly used configuration in industry for large area applications. In the design of such a reactor, special care must be taken in order to obtain the required film thickness homogeneity. Some considerations include the configuration of the RF electrode connections, the flow distribution of the supply gas and the reactor pumping, powder contamination, electrode topology and plasma uniformity near the electrode edges.

Experiment

The plasma reactor presented in Fig. 1 is a modified version of the industrial KAI-S type reactor commercialized by Balzers AG for thin-film deposition. It consists of a rectangular plasma reactor (57 cm x 47 cm) installed inside a larger vacuum chamber. The RF power is capacitively coupled to the RF electrode via a matching network at the input of which the forward and reflected power are measured. The interelectrode RF voltage distribution across the electrode surface in the plasma zone was measured in the absence of plasma with a passive RF voltage probe connected to a floating oscilloscope. The film thickness uniformity was measured by *ex situ* global interferometry by illuminating the substrate with a homogenous white light source and recording the transmitted light through a 700 nm interference filter. Each interference fringe indicates a 80 nm change in the film thickness. The *in situ* deposition rate was measured using a laser interferometer. For powder contamination investigations, the beam-expanded polarised light from an Argon ion laser was scattered from particles and monitored by a CCD camera. For this study, the scattered intensity was simply used as an indicator for the powder quantity. The excitation frequency was varied from 13.56 MHz to 70 MHz. Plasma parameters relevant to the deposition of amorphous silicon were chosen, namely, a 100 sccm flow of silane with a pressure of 0.2 Torr and a reactor temperature of 200°C.

RF voltage uniformity:

For RF frequencies, due to the skin effect, the RF current is confined to a thin surface layer. The RF electrode is therefore a double-skinned electrode in which the RF current continuity between the top and bottom surfaces is via the edge of the RF electrode. The problem of calculating the RF voltage distribution across the electrode area in the complex geometry of the real reactor is then reduced to a driven, two-dimensional Helmholtz equation applied to an equivalent unfolded two-dimensional geometry with periodic boundary conditions. An analytical solution based on the Green function technique was found for our particular rectangular geometry [1]. The

physical understanding afforded by the analytical approach shows that the principal non-uniformity is due to a logarithmic singularity in the vicinity of the RF and the ground connections. This singularity

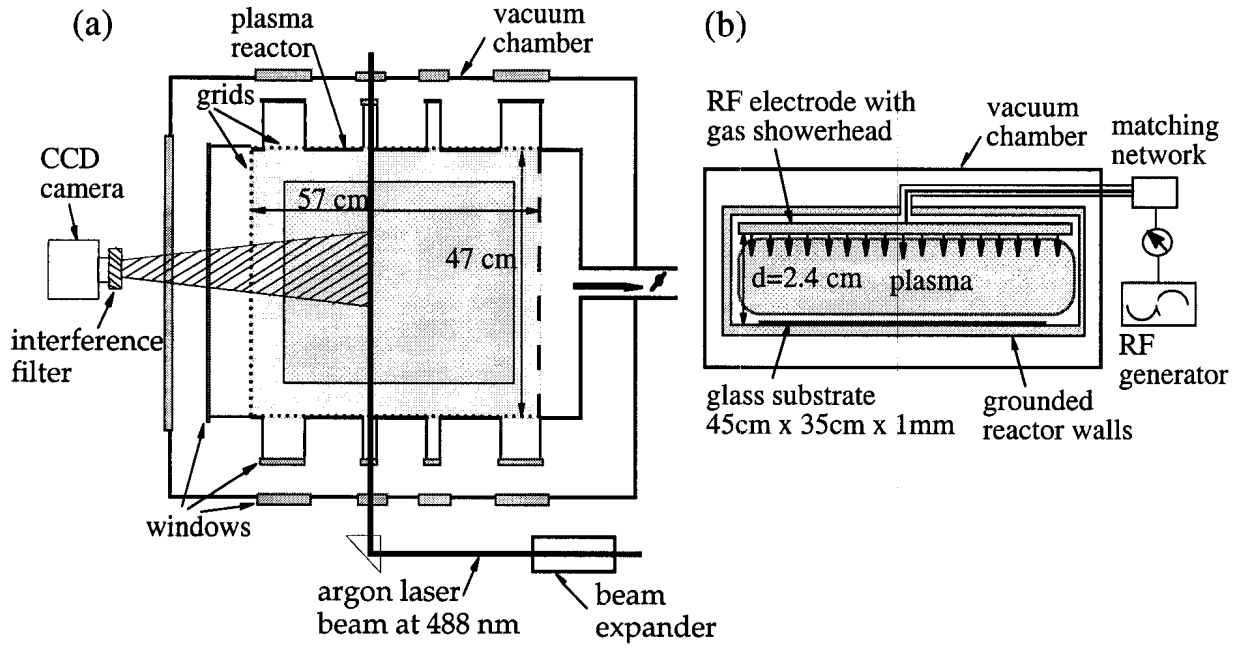

Figure 1: (a) Top view of the plasma reactor with diagnostics; (b) front view of the plasma reactor with the gas shower head.

is a property of the two-dimensional geometry and dominates the standing wave image of voltage distribution obtained from a one-dimensional transmission line model.
Fig. 2 shows the measured and calculated RF voltage distributions across the electrode area at 70 MHz for two different RF connection geometries. The edge RF connection geometry corresponds to the case with the RF connection located midway on the longer side of the RF electrode and the ground connection located on the corresponding side wall of the reactor, while the central RF connection geometry corresponds to the case with the RF connection centered on the top of the RF electrode and the ground connection located at the same place on the reactor cover as shown in Fig.1(b). For these two geometries, the calculated RF voltage distributions are in good agreement with the measurements. For the edge connection (Fig. 2 i)), the RF voltage amplitude strongly decreases towards the electrical connection location as predicted by the analytical two-dimensional model. For the central connection (Fig. 2 ii)), a good RF voltage uniformity is obtained. This is due to the fact that in this geometry the distance between the plasma zone and the singularity associated with the electrical connections is maximized. At 13.56 MHz, the reactor dimensions are well below a quarter of the wavelength and therefore the RF voltage was uniform even with the edge connection.
The film interferograms in Fig. 2 show the different film thickness uniformity obtained in each case. With the edge connection, the film thickness inhomogeneity was about ±38% while with the central top connection, the inhomogeneity was reduced below ±5%. The presence of a plasma does not short-circuit the voltage inhomogeneity. To conclude, RF voltage inhomogeneity is a major limiting factor for VHF plasma deposition in large surfaces.

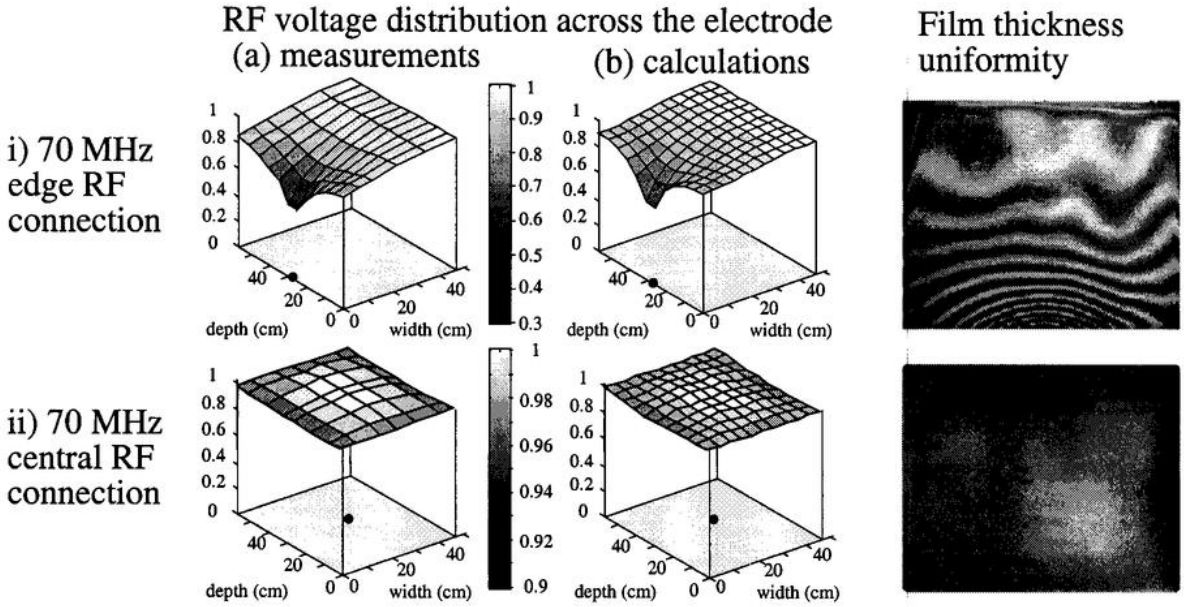

Figure 2: Measured and calculated interelectrode RF voltage distribution at 70 MHz for the edge and the central RF connection cases. The black point indicates the position of the RF and ground connections. The film interferograms show the uniformity of the film thickness for each case.

Influence of the gas flow on uniformity

The gas flow distribution in the reactor is another key parameter that will affect the deposition uniformity. Essentially two types of gas flow arrangement are used in industry: the longitudinal flow reactor, and the showerhead reactor. Uniform deposition rate and film composition are difficult to achieve in the longitudinal flow reactor because the working gas is more and more depleted in the direction of the gas flow and, therefore, the composition of the gas depends on the position in the reactor. This non-uniformity of the gas composition causes inhomogeneities in the deposition rate and in the film composition. On the other hand, the solution of the one-dimensional transport equations for plasma deposition in a uniform showerhead reactor [2] shows that the density of each neutral species is constant along the reactor. The plasma and surface reactions are then seen to be independent of position in any showerhead reactor with single-side pumping, which is a prerequisite for uniform deposition. This conclusion is valid for any degree of depletion: for a showerhead reactor, even plasma processes which involve total depletion of any supply gas can still result in uniform deposition

Non uniform deposition due to powder suspended in the plasma

Particles formed during silane plasma processing by plasma state polymerisation are a source of contamination. They are negatively-charged due to electron-ion flux equilibration at their surface and so are trapped by the plasma sheath potentials and accumulate in electrostatic suspension between the electrodes. Even if the film is not damaged by particles which fall onto the growing surface, the powder clouds suspended in the plasma above the growing film can cause inhomogeneous deposition by locally changing the plasma power dissipation, electron density and energy distribution. For example, films deposited at low input power show a very good uniformity but at a low deposition rate, whereas films deposited at higher input power with

powder formation have a higher deposition rate, but with a strongly degraded uniformity [3]. The inhomogeneities tend to be concentrated at the edges of the substrate where the thickness increases rapidly over the last 3 cm. The scattered intensity profiles in Fig. 3 show clear differences with and without substrate and it would appear that the substrate greatly influences the powder traps.

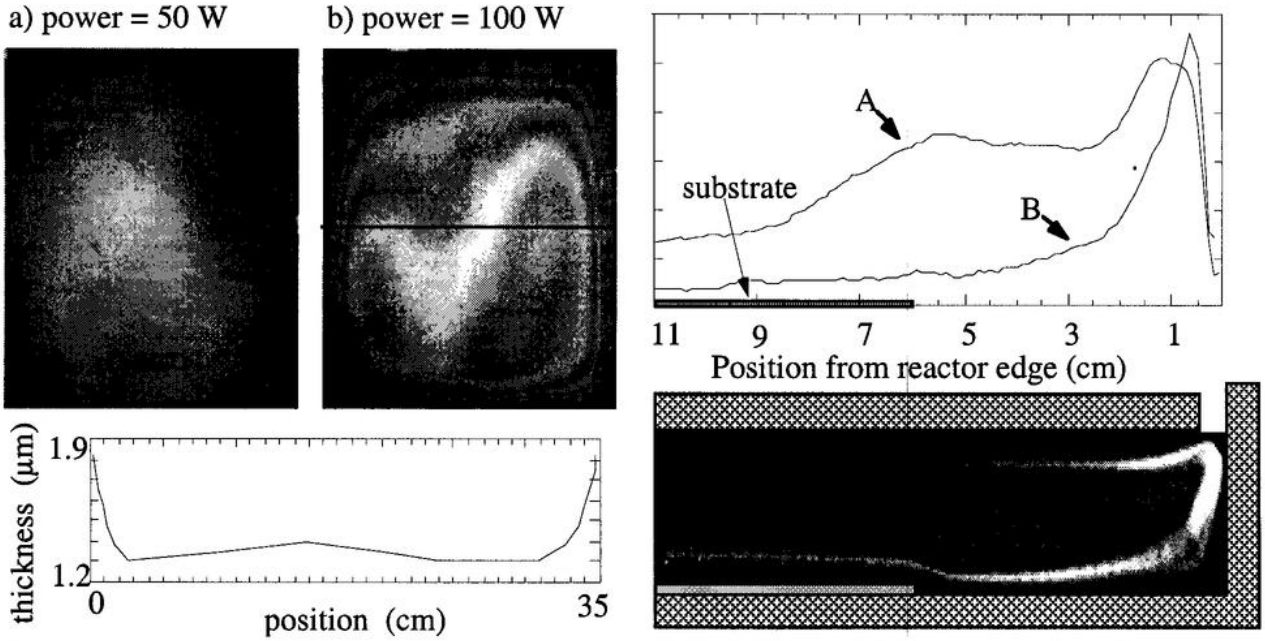

Figure 3: Global interferograms for films deposited a) at 50 W (no powder observed); and b) 100 W input power (with powder). The thickness profile corresponds to film b) along the line shown. Curve A represents the vertically-integrated intensity scattered from the powder measured from the CCD image shown; curve B is for the case without substrate.

Conclusions

Deposition uniformity has been considered from the point of view of RF voltage, gas flow and powder contamination. Further improvements are to be expected from current investigations into RF multi-point connections and segmented electrodes, generalised showerhead and pumping configurations, and novel design of the electrode edge geometry.

Acknowledgments

This work was funded by Swiss Federal Research Grants BBW 93.0136 (for Brite-Euram project BE-7328) and BEW 9400051.

References

[1] L. Sansonnens, A. Pletzer, D. Magni, A. A. Howling, Ch. Hollenstein, and J. P. M. Schmitt, Plasma Sources Sci. Technol. **6**, 170 (1997).

[2] L. Sansonnens, A. A. Howling, Ch. Hollenstein, Plasma Sources Sci. Technol. **9**, 205 (2000).

[3] Ch. Hollenstein, A. A. Howling, C. Courteille, J.-L. Dorier, L. Sansonnens, D. Magni and H. Muller, Mat. Res. Symp. Proc. **507**, 547 (1998).

Evidence for role of magnetic entropy in stationary Ohmic tokamak discharges

H. Weisen and E. Minardi*
Centre de Recherches en Physique des Plasmas
Association EURATOM - Confédération Suisse

**Istituto di Fisica del Plasma "P. Caldirola"*
Associazione EURATOM-ENEA-CNR, Milano, Italy

INTRODUCTION

Profiles from a large variety of stationary Ohmic plasmas in the TCV tokamak ($B_T<1.5T$, $R_0=0.88m$, $a<0.25m$, $\kappa<2.7$) are compared to theoretical predictions based on the assumption that the magnetic entropy is stationary in a tokamak considered as an open system interacting with the Ohmic transformer. For each value of $\langle j\rangle/(q_0 j_0)$, where $\langle j\rangle$ is the cross sectional averaged current density, and q_0, the theory predicts a rigid current profile in the confinement zone ($q>1$). Integration of the force balance equation leads to a restriction of the range of possible pressure profiles.

We observe that the sawtooth inversion radius and the electron temperature in the confinement region, related to the predicted rigid current profile using the neoclassical Ohm's law, depend solely on the parameter $\langle j\rangle/(q_0 j_0)$, in agreement with the predictions. The stiffness of the temperature profile, which follows from the rigid current profile, implies a correlation between density and pressure profiles, which is also observed in the experiment.

This agreement indicates that, contrary to widespread expectance, statistical concepts such as the magnetic entropy, can be of relevance to systems driven far from thermodynamical equilibrium, such as tokamak plasmas. The theory, as it stands, does however not provide a complete description of the behaviour of the pressure and density profiles. It makes no prediction as to the scaling of pressure profiles with $\langle j\rangle/(q_0 j_0)$, although such a scaling is also observed in the experiments, indicating that additional physics will need to be incorporated.

THEORY SUMMARY

Magnetic entropy is defined as a measure of probability of current density configuration in a suitably constrained space of magnetic equilibria [1,2].

$S \propto -\int \vec{j}^2 dV + \frac{\mu^2 c}{4\pi}\int \vec{j}\cdot\vec{A}\,dV$, $\vec{A}$ being the vector potential and $\vec{j}$ the current density.

In a plasma interacting with an Ohmic transformer the time variation of S is:

$$\frac{dS}{dt} \propto \int_V \left[\frac{\vec{E}}{\mu^2}\cdot\nabla^2\vec{j} + \vec{E}\cdot\vec{j}\right] dV$$

μ is a free parameter with the meaning of a Lagrange multiplier and $\vec{E}$ the induced electric field. In view of the arbitrariness of the integration volume V, the requirement of stationary entropy provides an equation for the steady-state toroidal current density profile:

$$\nabla^2\vec{j} + \mu^2\vec{j} = 0$$

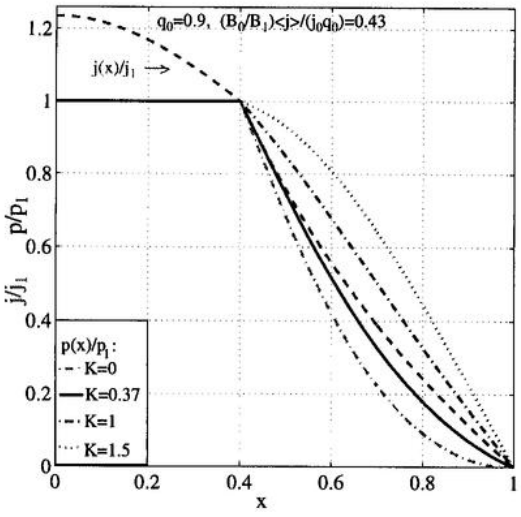

Fig.1 Theoretical current profile (dashed) and examples of pressure profiles with different values of convexity

Since the sawtoothing core is not stationary, we apply the above equation to the confinement zone only. For given $j=j_1$ at $r_1=r(q=1)$, it yields a rigid current profile in cylindrical geometry, for $r>r_1$ (fig.1):

$$j(r) = j_1[J_0(\mu a)Y_0(\mu r) - Y_0(\mu a)J_0(\mu r)]/D,$$

where $D = J_0(\mu a)Y_0(\mu r_1) - Y_0(\mu a)J_0(\mu r_1)$.

Assuming a parabolic q profile for $r<r_1$, $j_1 = j_0 q_0^2 (B_1/B_0)$, where B_1 and B_0 are the toroidal field on the $q=1$ surface and the axis, the theory relates q_0, q_a, and $\rho_1=r_1/a$. Combined with the Grad-Shafranov equation and an energy principle, the theory also restricts the range of possible pressure profiles [3]. For each q_0, r_1, there is a family of possible $p(r)$ parameterised by K $(0<K<1)$ and differing in their degree of concavity.

COMPARISON WITH TCV OHMIC DATABASE

The 280 discharges investigated include almost the entire range of sawtoothing Ohmic plasmas that can be produced in TCV, with $1<\kappa_a<2.54$, $-0.5<\delta_a<0.7$, $2<q_{95}<7$, $100kA<I_p<1.02MA$, $1.2\cdot10^{19}m^{-3}<\bar{n}_e<1.2\cdot10^{20}m^{-3}$ and $0.1<\nu^*_{75}<10$. The confinement properties of these discharges have been presented previously [4]. Since the theory is derived for circular cross sections only, we need to find a cylindrical equivalent to q_a. Theory suggests that the appropriate parameter is $B_0\langle j\rangle/(q_0 j_0 B_1) \cong \langle j\rangle/(q_0 j_0)$ as introduced in a previous study on sawtooth inversion radii and profile peaking factors [5]. For each sample in the database we construct a theoretical cylindrical model with the same value of $\langle j\rangle/(q_0 j_0)$ and (less importantly) the same value of β_p. The radial coordinate $x=r/a$ is identified with $(V/V_{tot})^{1/2}$. The parameter μ was set to $0.1/a$ and does not in effect play the role of a free parameter because for $\mu a<1$, the predictions are in practice equivalent.

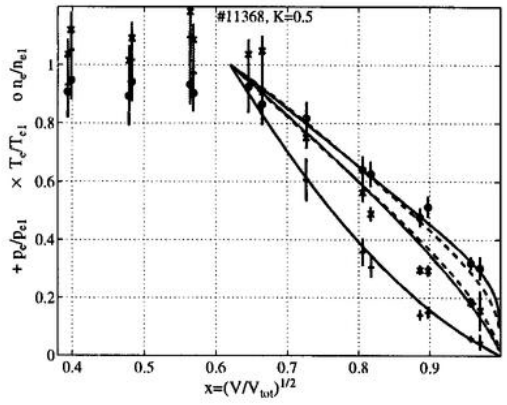

Fig.2 Measured profiles of electron temperature, pressure and density, together with theoretical profiles in the confinement zone. (dashed: Spitzer conductvity assumed)

Using the neoclassical Ohm's law, the predicted, Ohmically relaxed current profile can be related to a temperature profile, shown in red together with the pressure (black) and density profiles (blue) for an example of a TCV discharge in fig.2. These profiles are from a pulsed Thomson scattering diagnostic which is not synchronised with the sawtooth cycle. All profiles are normalised to their values at the inversion radius. The fitted line for the pressure profile corresponds in this example to a theoretical pressure profile with a convexity parameter $K=0.5$. The resulting line for the density profile is obtained by combining the theoretical electron temperature and pressure profiles.

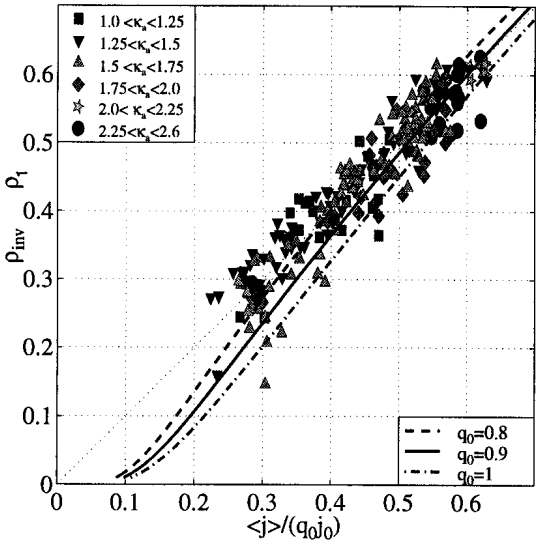

Fig.3 Measured normalised sawtooth inversion radii together with predicted positions for q=1 radii for three assumed values of q_0. Symbols relate to elongation.

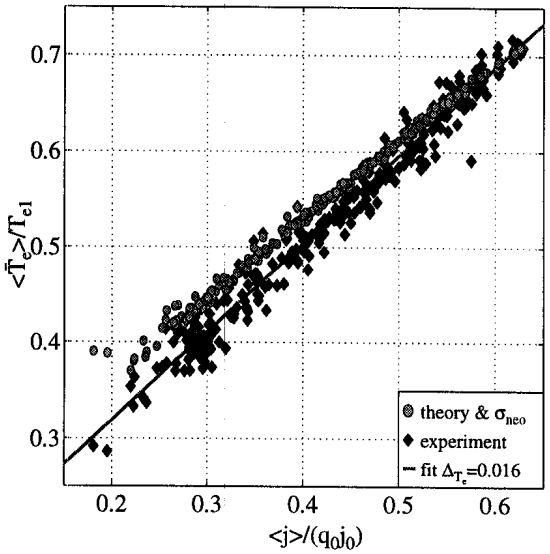

Fig.4 Scaling with $\langle j\rangle/q_0 j_0$ of electron temperature profile shape factors in confinement zone.

Predictions for $\rho_1(q_0, \langle j\rangle/(q_0 j_0))$ agree well with the observed inversion radius from X-ray tomography [5], for the generally accepted values for q_0 in sawtoothing plasmas ($0.8<q_0<1$), as seen fig. 3. For the remainder of the paper we assume $q_0=0.9$. A systematic comparison of profile shapes in the confinement zone is made by defining "clipped profiles" such as $\overline{T}_e/T_{e1}$, where $\overline{T}_e = max(T_e, T_{e1})$ which in effect disregards the reheating inside the inversion radius after the core has been flattened by a sawtooth crash (fig.4). The quantity $\langle\overline{T}_e\rangle/T_{e1}$ has the advantage of being sensitive only to the profile shape for $r>r_1$ and does not depend on the time at which the Thomson scattering measurements are taken, because plasma parameters near the inversion radius vary relatively little during the sawtooth cycle.

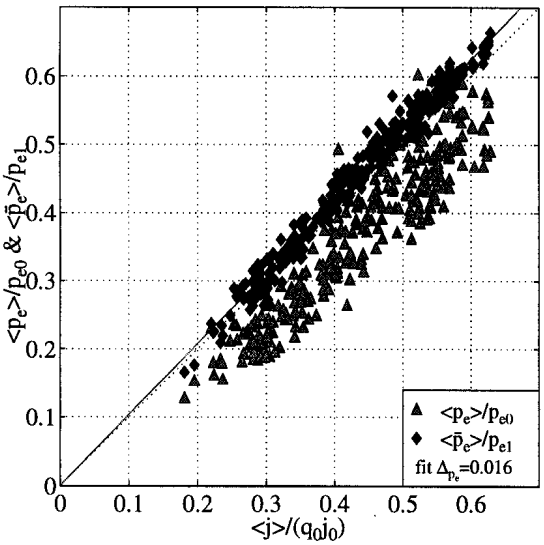

Fig.5 Scaling of experimental pressure profile factors with $\langle j\rangle/q_0 j_0$.

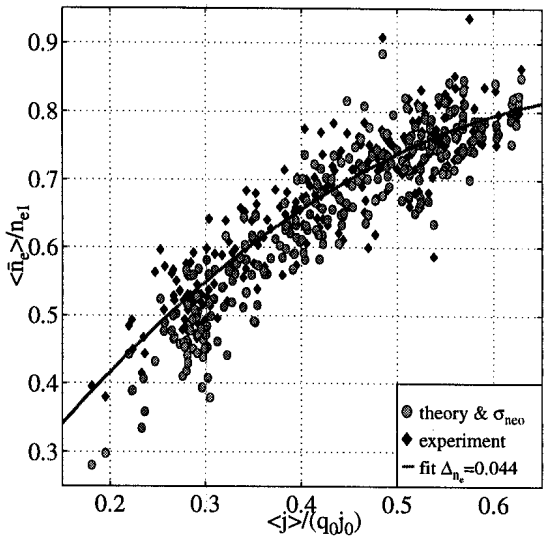

Fig.6 Scaling of experimental and expected density profile factors.

Fig.4 shows that the measured shape of the temperature profile (diamonds) in the confinement zone is in good agreement with the one expected from the theoretical current profile and Ohm's law (dots). The scaling with $\langle j\rangle/(q_0 j_0)$ of the experimental pressure profile factors $\langle \bar{p}_e\rangle/p_{e1}$ (diamonds) and $\langle p_e\rangle/p_{e0}$ (triangles) are shown in fig. 5. The latter exhibit more scatter because of sampling at random times during the sawtooth cycle. Fig.6 shows that experimental density profile factors (diamonds) also scale with $\langle j\rangle/(q_0 j_0)$. The density profile widths expected from the theoretical current profile and the matching theoretical pressure profiles are shown as dots in fig.6.

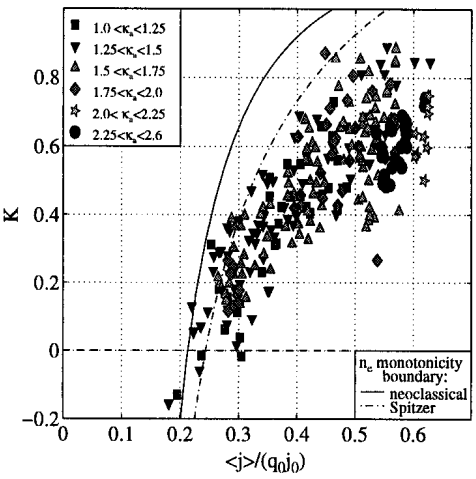

Fig.7 Convexity parameter K corresponding to experimental pressure profiles in fig.5.

The values of the theoretical convexity parameter corresponding to the pressure profiles in fig.5 (diamonds) are plotted in fig.7. There is a systematic trend, with K increasing from near zero at the lowest values of $\langle j\rangle/(q_0 j_0)$ to near *0.6* at the highest. This dependence is not predicted by the theory, which merely constrains K to be in the interval *[0,1]*. Pressure profiles with K larger than the curves plotted in fig.7 would correspond to hollow density profiles. The absence of high values ok K at low values of $\langle j\rangle/(q_0 j_0)$ may be explainable if the plasma lacks a mechanism to set up the required outward particle drift over part of the cross section. In any case, a more complete description is likely to require the integration of additional physics concerning particle and/or energy transport.

In figs. 4-6 we show the experimental average scaling of shape factors as solid lines. It is interesting to note that departures from the average correlate for density and pressure, while temperature profile deviations remain uncorrelated with the former two and can be attributed to measurement errors. Such behaviour is expected from stiff temperature profiles (fig.8), such as predicted by the theory presented [3].

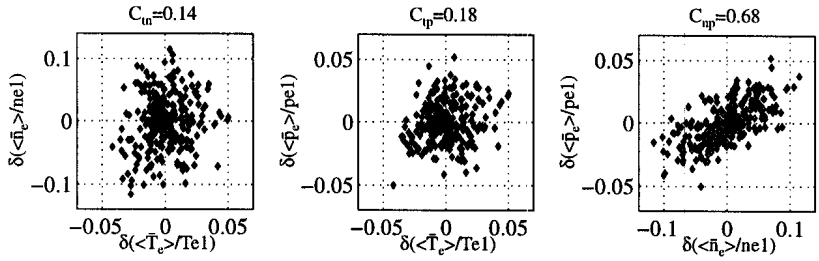

Fig.8 Cross correlations of profile shapes in ohmic database.

Acknowledgement: This work was partly supported by the Swiss National Science Foundation. The support of the entire TCV team is gratefully acknowledged.

References

[1] E. Minardi, J. Plasma Physics **48** (1992) 281
[2] E. Minardi, J. Plasma Physics **62** (1999), 319
[3] E. Minardi and H.Weisen, submitted to NF (2000), CRPP report LRP 669/00.
[4] H. Weisen et al, Plasma Phys. Contr. Fusion **39** (1997) B135
[5] H. Weisen et al, Plasma Phys. Contr. Fusion **40** (1998) 1803